Progress in Neurobiology 231 (2023) 102530

Contents lists available at ScienceDirect

Progress in Neurobiology

journal homepage: www.elsevier.com/locate/pneurobio

TRPM2 as a conserved gatekeeper determines the vulnerability of DA neurons by mediating ROS sensing and calcium dyshomeostasis

Peiwu Ye [a,1], Qiuyuan Fang [a,1], Xupang Hu [b,1], Wenjuan Zou [c,1], Miaodan Huang [d], Minjing Ke [d], Yunhao Li [d], Min Liu [a], Xiaobo Cai [a], Congyi Zhang [a], Ning Hua [a], Umar Al-Sheikh [c], Xingyu Liu [a], Peilin Yu [e], Peiran Jiang [f], Ping-Yue Pan [g], Jianhong Luo [f], Lin-Hua Jiang [h,i,l], Suhong Xu [j], Evandro F. Fang [k], Huanxing Su [d,*], Lijun Kang [b,f,**], Wei Yang [a,*]

[a] Department of Biophysics, Institute of Neuroscience, NHC and CAMS Key Laboratory of Medical Neurobiology, Zhejiang University School of Medicine, Hangzhou 310058, China
[b] Second Clinical Medical College, Affiliated Secondary Hospital, Zhejiang Chinese Medical University, Hangzhou, Zhejiang 310011, China
[c] Department of Neurobiology and Department of Neurosurgery of the First Affiliated Hospital, Zhejiang University School of Medicine, Zhejiang 310053, China
[d] Institute of Chinese Medical Sciences, University of Macau, Macau, China
[e] Department of Toxicology, School of Public Health, Zhejiang University, Hangzhou, Zhejiang 310058, China
[f] School of Brain Science and Brain Medicine, Zhejiang University, Hangzhou 310058, China
[g] Department of Neuroscience and Cell Biology, Rutgers University Robert Wood Johnson Medical School, 675 Hoes Lane, Piscataway, NJ 08854, USA
[h] School of Biomedical Sciences, University of Leeds, Leeds LS2 9JT, UK
[i] Sino-UK Laboratory of Brain Function and Injury of Henan Province, Department of Physiology and Neurobiology, Xinxiang Medical University, Xinxiang 453000, China
[j] Center for Stem Cell and Regenerative Medicine and Department of Cardiology of The Second Affiliated Hospital, Zhejiang University School of Medicine, 310058, Hangzhou, China
[k] Department of Clinical Molecular Biology, University of Oslo and Akershus University Hospital, Lørenskog, Norway
[l] University of Leeds, Leeds LS2 9JT, UK

ARTICLE INFO

Keywords:
Dopaminergic neurons
Vulnerability
TRPM2
Parkinson's Disease

ABSTRACT

Different dopaminergic (DA) neuronal subgroups exhibit distinct vulnerability to stress, while the underlying mechanisms are elusive. Here we report that the transient receptor potential melastatin 2 (TRPM2) channel is preferentially expressed in vulnerable DA neuronal subgroups, which correlates positively with aging in Parkinson's Disease (PD) patients. Overexpression of human TRPM2 in the DA neurons of *C. elegans* resulted in selective death of ADE but not CEP neurons in aged worms. Mechanistically, TRPM2 activation mediates FZO-1/CED-9-dependent mitochondrial hyperfusion and mitochondrial permeability transition (MPT), leading to ADE death. In mice, TRPM2 knockout reduced vulnerable substantia nigra pars compacta (SNc) DA neuronal death induced by stress. Moreover, the TRPM2-mediated vulnerable DA neuronal death pathway is conserved from *C. elegans* to toxin-treated mice model and PD patient iPSC-derived DA neurons. The vulnerable SNc DA neuronal loss is the major symptom and cause of PD, and therefore the TRPM2-mediated pathway serves as a promising therapeutic target against PD.

1. Introduction

Dopaminergic (DA) neurons play an important role in the regulation of voluntary movement, emotion and reward in vertebrates, including Homo sapiens and rodents (Schultz, 2007; Ungless and Grace, 2012). A majority of DA neurons located in the ventral midbrain (VM) are produced in the basal region of the midbrain during embryonic development. Midbrain DA neurons are classified into three anatomically and

* Corresponding authors.
** Corresponding author at: Second Clinical Medical College, Affiliated Secondary Hospital, Zhejiang Chinese Medical University, Hangzhou, Zhejiang 310011, China.
E-mail addresses: huanxingsu@umac.mo (H. Su), kanglijun@zju.edu.cn (L. Kang), yangwei@zju.edu.cn (W. Yang).
[1] These authors contributed equally.

https://doi.org/10.1016/j.pneurobio.2023.102530
Received 11 June 2023; Received in revised form 1 September 2023; Accepted 17 September 2023
Available online 20 September 2023

functionally distinct clusters, termed the retrorubral area (RR), the substantia nigra pars compacta (SNc) and the ventral tegmental area (VTA), with SNc and VTA consisting most of the DA neurons (Anderegg et al., 2015). Similarly, DA neurons in *Caenorhabditis elegans (C. elegans)*, a canonical model organism used to investigate mechanisms of human diseases, are composed of three anatomically distinct subtypes, including two Anterior DEirid (ADE), four CEPhalic sensory (CEP), and two Posterior Deirid (PDE) neurons. These three subtypes of ciliated DA neurons function redundantly in modulating decreased moving speed behavior in response to food and mechanosensation (Sawin et al., 2000). Therefore, the diversity among DA neuronal subgroups is conserved from model animals to human.

DA neuron subtypes share the common DA neuronal markers, such as tyrosine hydroxylase (TH) and dopa decarboxylase (DDC) required for dopamine synthesis, but some DA neuron clusters exhibit greater susceptibility to damage by stress than others, with a well-known example being that the degeneration of DA neurons in the SNc, but not those in the VTA, is most prominent in the brains of Parkinson's Disease (PD) patients (Damier et al., 1999; Hirsch et al., 1988). Exposure to the metabolite of 1-methyl-4-phenyl-1,2,3,6-tetrahydropyridine (MPTP), a neurotoxin known to induce PD-like phenotypes, results in preferential loss of SNc neurons in mice (Di Salvio et al., 2010; Liss et al., 2005). A previous study also showed that some but not all DA neurons degenerate in transgenic Drosophila expressing α-synuclein (Feany and Bender, 2000), suggesting that differential vulnerability is conserved across species. *C. elegans* is a widely used model organism to examine the mechanisms driving human neurodegenerative diseases (Fang et al., 2019; Sorrentino et al., 2017), but whether DA neurons in this model organism display differential vulnerability to stress remains unknown.

In the last few decades, a consensus has been reached that the selective vulnerability of SNc neurons is mainly caused by their high bioenergetic demands, such as pacemaking activity (Surmeier, 2007), high DA- and iron-related toxicity (Hare and Double, 2016; Segura-Aguilar et al., 2014), and possessing a highly complex axonal arborization (Bolam and Pissadaki, 2012; Matsuda et al., 2009; Pacelli et al., 2015; Parent and Parent, 2006). So far, the molecular mechanism responsible for the differential vulnerability of DA neuron clusters is however largely unclear. Recent studies taking advantages of transcriptomics have attempted to identify the marker genes and uncovered cellular heterogeneity of DA neurons (Chung et al., 2005; Grimm et al., 2004; Kamath et al., 2022; Tiklova et al., 2019), which is crucial for understanding the molecular cascades underpinning the selective vulnerability of DA neurons. For example, invulnerable VTA DA neurons are enriched with transcripts for neuroprotective proteins like PACAP, BMP (MPTP-resistance), ANP (anti-oxidative stress) and PARM-1 (anti-apoptosis) (Grimm et al., 2004). SnRNA-seq analysis of DA neurons from postmortem human SNc indicates the AGTR1-positive DA neurons located in the ventral tier of SNc are highly vulnerable (Kamath et al., 2022). However, the functions of the differentially expressed genes in mediating vulnerability have not yet been experimentally verified.

Here we have found that the expression of TRPM2 channel shows a positive correlation with aging and it is preferentially enriched in vulnerable DA neurons, raising the possibility that TRPM2 mediates the vulnerability of DA neurons. To test this hypothesis, we constructed a transgenic *C. elegans* strain with human TRPM2 (hTRPM2) specifically expressed in DA neurons. Interestingly, hTRPM2 expression selectively confers vulnerability to ADE rather than CEP neurons. Mechanistically, TRPM2 is preferentially activated by ADP-ribose (ADPR) and reactive oxygen species (ROS) that promotes ADPR production via poly(ADPR), polymerase (PARP) and poly(ADPR) glycohydrolase (PARG) in ADE neurons and promotes mitochondrial hyperfusion via the FZO-1/CED-9-complex, leading to ADE neuronal death. The TRPM2 channel also mediates the vulnerability of SNc DA neurons in MPTP-induced PD mice through Mfn2/Bcl-2, the homologues of worm FZO-1/CED-9. Furthermore, blockage of the TRPM2-mediated DA neuronal death pathway prevents the demise of DA neurons differentiated from sporadic PD (SPD) patient-specific induced pluripotent stem cells (iPSC). Taken together, these findings uncover TRPM2 as an important mechanism mediating the vulnerability of DA neurons that is conserved across different species.

2. Results

2.1. TRPM2 is enriched in vulnerable DA neuron clusters

A previous study conducted single-cell transcriptome sequencing in iPSC-differentiated DA neurons and characterized the composition and cell-type specific responses to genetic and cytotoxic stress (ArrayExpress Accession Number: E-MTAB-9154) (Fernandes et al., 2020). We re-analyzed the data from untreated- and rotenone-treated groups and categorized the differentiated neurons into six clusters (DAn1–6) (Fig. 1 A), and the DAn1 cluster shows significant neuronal loss (Fig. 1B), indicating its vulnerability. The G-protein gated inwardly-rectifying K^+ channel subunit (GIRK2, encoded by KCNJ6 gene) is reported to be the marker gene of SNc DA neurons, and calbindin (encoded by CALB1 gene) is the marker of VTA neurons in mammalian brains (Thompson et al., 2005). Our results showed that GIRK2 rather than calbindin is abundantly expressed in the vulnerable DAn1 cluster (Fig. 1 C and D), suggesting that the iPSC-derived DAn1 neuron cluster may be as vulnerable as the SNc DA neurons in human brain. Previous studies have demonstrated that SNc neurons rather than VTA neurons maintain high levels of oxidative stress and Ca^{2+} entry activity, which is suggested to play a vital role in determining the vulnerability of SNc DA neurons (Guzman et al., 2010). Thus, we examined the expression and distribution of transient receptor potential (TRP) ion channels that are known to be capable of detecting alterations in cellular redox status and mediating Ca^{2+} influx, including TRPM2, TRPC5 and TRPA1 (Jiang et al., 2018; Maddox et al., 2018; Takahashi et al., 2011). The results showed that only TRPM2 is preferentially enriched in the vulnerable DAn1 cluster (Fig. 1E). To further verify this finding, we also analyzed the expression of TRPM2 based on three other public databases. The TRPM2 expression profile in the midbrain obtained from the Human Protein Atlas Dataset (www.proteinatlas.org) showed that the expression of TRPM2 in the SNc region is higher than in the VTA region, regardless of gender (Supplementary Fig. 1A-C). We also analyzed the expression of TRPM2 in SNc neurons from a single-cell transcriptomic atlas of human SNc in PD patients (Wang et al., 2022). The results suggest that TRPM2 expression displays a positive correlation with aging in PD patients (Fig. 1 F and G). A recent study has identified a subpopulation of vulnerable DA neurons (AGTR1- and SOX6-positive) based on single-cell sequencing of human ventral tier SNc DA neurons (Fig. 1H, NCBI GEO Accession Number: GSE178265) (Kamath et al., 2022). We found that GIRK2 and TRPM2 rather than calbindin are more enriched in this vulnerable neuron cluster (Fig. 1I-K). To verify these RNA-seq-based data, we detected the expression of TRPM2 in mouse midbrain via RNA-scope. The results indicate that the mRNA level of TRPM2 in aged mice is indeed significantly higher in the ventral tier of SNc DA neurons than that in VTA (Fig. 1 L and M), consistent with the above-described results from RNA-seq-based analysis. The Ca^{2+}-permeable TRPM2 channel is known as an oxidative stress sensor for it is activated by ROS via the PARP/PARG/ADPR axis in synergy with Ca^{2+} (Huang et al., 2018; Wang et al., 2018; Yu et al., 2019; Yu et al., 2017; Yu et al., 2021). Therefore, we propose TRPM2 as a mechanism mediating DA neuronal vulnerability to stress.

2.2. Ectopic expression of hTRPM2 in C. elegans induces selective DA neuronal degeneration

There is no homologue of TRPM2 in *C. elegans*, and previous studies did not observe preferential loss of DA neurons in various neurodegeneration models of *C. elegans* carrying genetic mutation, or upon

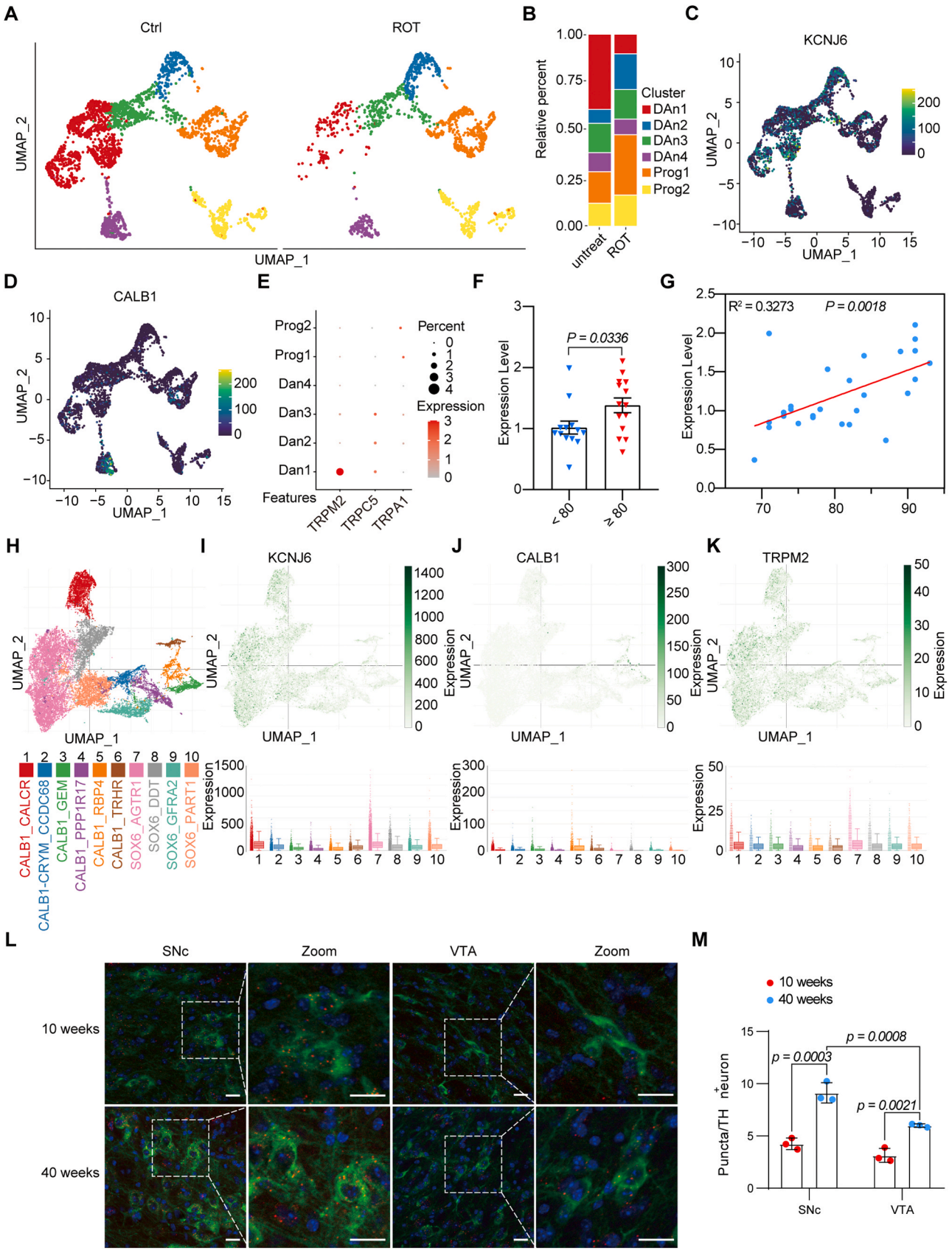

Fig. 1. TRPM2 is enriched in vulnerable DA neuron clusters.

α-synuclein overexpression or treatment with toxins (Chikka et al., 2016; Lakso et al., 2003; Nagarajan et al., 2014). To explore whether TRPM2 indeed endows the DA neurons with vulnerability in worms, we constructed *C. elegans* strains independently and specifically expressing hTRPM2 and DsRed fluorescent protein in DA neurons under the control of *Pdat-1* promoter (Supplementary Fig. 2A-D). Interestingly, following TRPM2 expression, ADE, PDE neurons and CEP neurons showed completely different phenotypes. Both ADE and PDE neurons in hTRPM2-expressing worms exhibited substantial neurodegeneration, characterized by progressive loss of the process carrying bubbles and the cell body within 7 days from adult day 1 (Fig. 2A-B and Supplementary Fig. 2E and F). In contrast, CEP neurons from the same worms remained unaffected, even on adult day 7 and day 10 (Fig. 2 A and B and Supplementary Fig. 2 G). Thus, only ADE and PDE in *C. elegans* become highly vulnerable as a result of TRPM2 expression. Due to an age-related increase in autofluorescence of the gut that severely confounds the quantification of PDE neurons, we focused on the ADE and CEP neurons in the following studies.

To determine whether the selective vulnerability of DA neurons in *C. elegans* conferred by ectopic expression of hTRPM2 arose from the difference in hTRPM2 channel function in ADE and CEP neurons, we conducted in vivo electrophysiological recordings of hTRPM2-mediated currents in response to application of a saturation concentration of ADPR and Ca^{2+} used in previous studies (Singatulina et al., 2019; Vyas et al., 2014). ADE and CEP neurons from hTRPM2-expressing worms responded to administration of ADPR/Ca^{2+} with similar current amplitudes (Supplementary Fig. 2H and I), indicating that TRPM2 is functionally expressed at a similar level in ADE and CEP neurons. In contrast with expression of the wildtype (WT)-hTRPM2, expression of the hTRPM2 mutant carrying E960Q in the pore region that reduces the Ca^{2+}-permeability or R1433A in the C-terminal containing ADPR-binding pocket (Xia et al., 2008; Yu et al., 2017) dramatically reduced ADE neuronal death (Fig. 2C-E), albeit similar expression of TRPM2 in these two mutant strains, suggesting that induction of selective degeneration of ADE DA neurons by ectopic expression of hTRPM2 is dependent on the channel activity.

We also treated worms with MPP^+, the neurotoxic MPTP that inhibits NAD(H)-linked mitochondrial oxidation at the level of complex I of the electron transport system (Nicklas et al., 1987). The results showed that treatment with MPP^+ exacerbated ADE neuronal death in TRPM2-expressing worms in comparison to WT worms (Supplementary Fig. 2 J), while cause similar toxic effect on CEP neurons(Supplementary Fig. 2 J). These results suggest it is ADE rather than CEP that contributes to the vulnerability of DA neurons.

TRPM2 is a Ca^{2+}-permeable channel mediating Ca^{2+} influx and, as introduced above, intracellular Ca^{2+} is an important factor responsible for TRPM2 activation. To verify the role of Ca^{2+} in hTRPM2 expression-induced ADE neuron degenerating pathway, we firstly measured the cytosolic Ca^{2+} level in ADE and CEP neurons on day 1 using GCaMP3 (Xu and Chisholm, 2014). The results showed that the cytosolic Ca^{2+} level was much higher in ADE neurons than CEP neurons in hTRPM2-expressing worms (Supplementary Fig. 3 A). Application of the Ca^{2+} chelator BAPTA-AM significantly suppressed ADE neuronal death in hTRPM2-expressing worms (Supplementary Fig. 3 C and D), providing further evidence to suggest the critical engagement of Ca^{2+} overload in hTRPM2 expression-induced ADE neurodegeneration. We next examined the ROS level, which not only induces TRPM2 activation, but also results in neuronal damage during pathogenesis (Di et al., 2011;

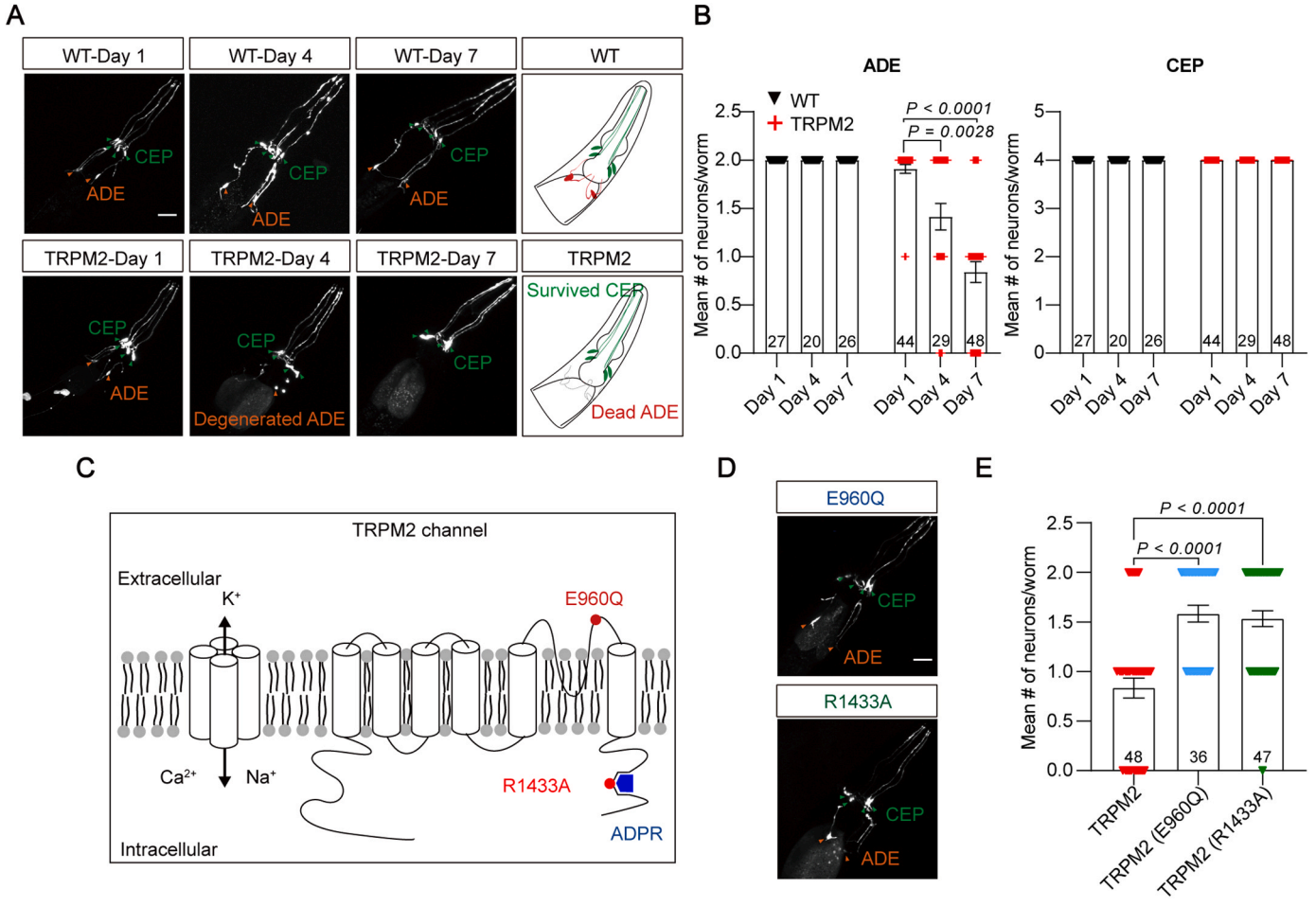

Fig. 2. Ectopic expression of hTRPM2 in C. elegans induces selective DA neuron degeneration.

Fanczal et al., 2020). By using Hyper, a ROS sensor (Markvicheva et al., 2011), we observed that the ROS level in ADE neurons was considerably higher than that in CEP neurons in hTRPM2-expressing worms (Supplementary Fig. 3B). Additionally, treatment with the ROS scavenger N-acetyl cysteine (NAC) modestly suppressed ADE neuronal death in hTRPM2-expressing worms (Supplementary Fig. 3 C and D). Taken together, these observations demonstrate that the selective vulnerability of ADE neurons upon hTRPM2 expression arises in part from the elevated levels of Ca^{2+} and ROS that activate hTRPM2 to drive neuronal death.

2.3. TRPM2 contributes to the vulnerability of SNc DA neurons in PD mice

To further validate the role of TRPM2 in mediating DA neuron vulnerability in mammalian animals, we used MPTP- and rotenone (Rot)-induced mouse PD models. Our results showed that treatment with MPTP induced degeneration of SNc without effect on VTA DA neurons in WT mice (Fig. 3A-B), and TRPM2 knockout (TRPM2-KO) significantly suppressed MPTP-induced loss of SNc DA neurons (Fig. 3A-B), confirming that TRPM2 is critical for mediating DA neuron vulnerability. Moreover, stereotaxic injection of rotenone into one side of the SNc region in mice led to apomorphine-induced rotation and decreased rotarod time (Fig. 3C-E), which mimics the behavior of PD patients.

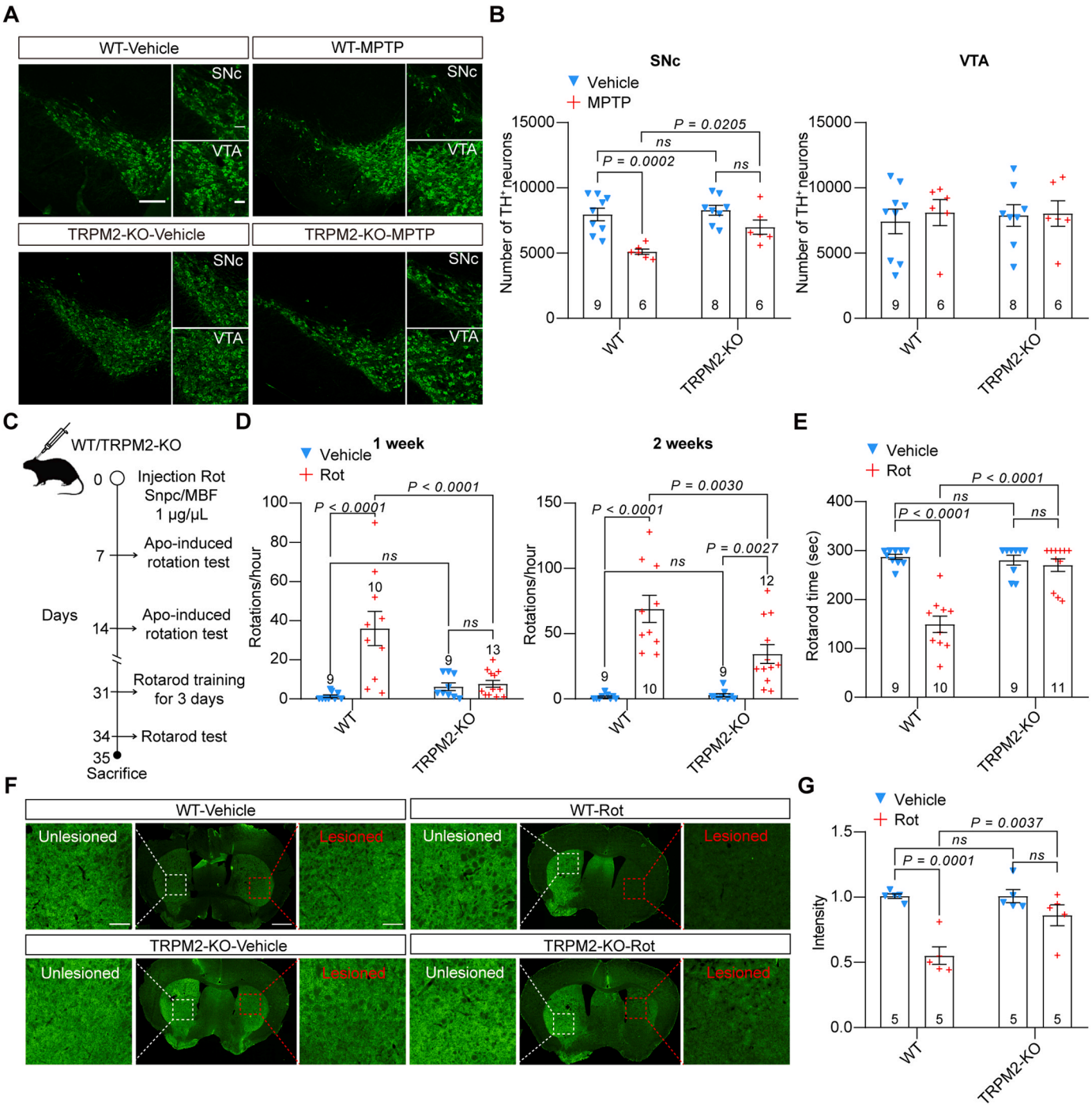

Fig. 3. TRPM2 contributes to the vulnerability of SNc DA neurons to stress in mice.

Furthermore, progressive dopaminergic axon degeneration was observed in the striatum a month following injection in the WT mice (Fig. 3C, F and G). Consistently, these motor deficits and pathological changes were significantly attenuated in the TRPM2-KO mice (Fig. 3D-G), further supporting that TRPM2 mediates SNc DA neuronal death. These results demonstrate that TRPM2-mediated vulnerability of SNc DA neurons is conserved across species.

2.4. TRPM2 induces ADE death through FZO-1/CED-9-mediated mitochondrial hyperfusion

We next examined whether TRPM2 induced ADE neuronal death through the core apoptosis machineries, including EGL-1, CED-9 (anti-apoptosis), CED-4 and CED-3 (Fig. 4 A) (Ellis and Horvitz, 1986). The hTRPM2-expressing worms were cross-bred with various mutant strains with loss-of-function *ced-4 (n1162)*/apoptotic protease activating factor-1 (Apaf-1), *egl-1* (n1084n3082)/BH-3, *ced-3 (n717)*/caspase, or gain-of-function *ced-9 (n1950)*/Bcl-2 that have been shown to prevent canonical apoptosis (Hengartner and Horvitz, 1994). Among these mutants, only loss-of-function *ced-4* in hTRPM2-expressing worms led to significant attenuation of ADE neuronal death (Fig. 4B and C and Supplementary Fig. 3E and F). Surprisingly, the loss-of-function *ced-9 (n2812)* mutant dramatically suppressed ADE neuron degeneration in hTRPM2-expressing worms, while the gain-of-function *ced-9* mutant failed to protect ADE neurons (Fig. 4B and C). These results indicate that hTRPM2 induced ADE neuronal death through CED-4 and CED-9.

Mitochondrial dysfunction is a well-known initiating factor in apoptosis and has paramount importance in stress-induced DA neurodegeneration. It was reported that mitochondria-located Bcl-2 family proteins play critical roles in regulating mitochondrial dynamics (Lu et al., 2011; Rolland et al., 2009). Thus, we next sought to explore the intriguing role of CED-9 by further investigating its contribution to mitochondrial dysfunction in the ADE neurons of hTRPM2-expressing worms. Confocal microscopy revealed that mitochondria in the ADE neurons showed increased mitochondrial length compared to those in the CEP neurons in the hTRPM2-expressing worms as well as in the WT worms (Fig. 4D and E). This finding was further corroborated by the 3-dimensional reconstruction analysis of mitochondrial morphology determined by using scanning electron microscopy (Fig. 4D), indicating mitochondrial hyperfusion or fission defect in hTRPM2-expressing ADE neurons. The mitochondrial morphology in hTRPM2-expressing worms was largely restored by the loss-of-function *ced-9 (n2812)* mutation (Fig. 4E and F), confirming that CED-9 contributes to hTRPM2-induced mitochondrial fusion/fission defects in ADE neurons.

Previous studies have reported that CED-9 promotes mitochondrial fission by interacting with EGL-1 and DRP-1, or mediates mitochondrial fusion by interacting with CED-4 and FZO-1 in *C. elegans* (Lu et al., 2011; Rolland et al., 2009). Nonetheless, such a mechanism remains debatable, for another study showed no involvement of CED-9 in mitochondrial dynamics (Breckenridge et al., 2009). Here, our data showed that there is no protective effect when the hTRPM2-expressing worms were cross-bred with the EGL-1 mutant strain (Supplementary Fig. 3E and F), suggesting that EGL-1/CED-9-mediated mitochondrial fission is not critically involved in ADE neuronal death. In contrast, knockdown of *fzo-1* rather than *drp-1* mitigated ADE neuron degeneration in the hTRPM2-expressing worms (Fig. 4 G and H). Consistently, expression of a CED-9-binding domain of FZO-1 (AA346–595, containing a coiled-coil domain) attenuated ADE neuron degeneration in the hTRPM2-expressing worms, which likely resulted from competitive blockade of the FZO-1/CED-9-mediated mitochondrial fusion (Fig. 4 G and H). These results support that mitochondrial hyperfusion mediated by the FZO-1/CED-9 complex plays a vital role in hTRPM2 expression-induced ADE neuron degeneration.

It has been reported that mitochondrial hyperfusion causes mitochondrial permeability transition (MPT) (Papanicolaou et al., 2011), resulting in cell death. Therefore, we examined whether MPT is involved in TRPM2-mediated neuronal death. Deletion of *cyn-1* which encodes the regulatory component of MPT in *C. elegans* reduced ADE neuronal death in the TRPM2-expressing worms (Supplementary Fig. 3E and F). Moreover, blocking the MPT pore opening with cyclosporin A (CsA) improved the viability of ADE neurons (Supplementary Fig. 3 C and D). These results indicate that the FZO-1/CED-9 complex formation driven by TRPM2 activation induces mitochondrial hyperfusion and that MPT contributes to ADE neuronal death in the hTRPM2-expressing worms.

To further determine whether such a novel role of the FZO-1/CED-9 complex in mediating DA neuronal death is conserved in mammalian animals, we analyzed the Mfn2/Bcl-2 (the homologue of FZO-1/CED-9 in mice) interactions in MPTP-treated PD mouse model. Using a Proximity Ligation Assay (PLA), we showed that TRPM2-KO significantly attenuated MPTP-induced Mfn2/Bcl-2 interactions in the SNc but not the VTA DA region (Fig. 4I and J), supporting the notion that TRPM2-induced Mfn2/Bcl-2 interaction is critical for selective SNc DA neuronal death. These results indicate that TRPM2-mediated Mfn2/Bcl-2 interaction indeed conservatively mediates the vulnerability of SNc DA neurons to stress in mice.

2.5. The PARP-1/PARG/ADPR axis mediates TRPM2 activation to induce selective ADE death

The above-described results show that hTRPM2 plays a novel role in determining DA neuron vulnerability, and we further investigated how TRPM2 selectively mediates ADE neuronal death using hTRPM2 transgenic *C. elegans*. ADPR acts as the major endogenous ligand of the TRPM2 channel, which is mainly synthesized by PARP, particularly PARP-1, and PARG responding to DNA damage (Fig. 5 A) (Qi et al., 2019; Vyas et al., 2014). To determine whether preferential TRPM2 activation is responsible for ADE death in *C elegans*, we firstly investigated the potential roles of PARP-1 and PARG in hTRPM2-induced selective ADE neuronal death. Overexpression of worm PARP-1 in DA neurons caused ADE cell death in WT animals and exacerbated ADE neuronal death in hTRPM2-expressing animals (Fig. 5B-C). Notably, it also resulted in significant CEP neuronal death (Fig. 5B-C). Consistently, knockdown of *parp-1* or *parg-1* dramatically suppressed ADE neuronal death in hTRPM2-expressing worms (Fig. 5B-C). Moreover, treatment with either the PARP-1 inhibitor PJ-34 (Szabo et al., 2002) or the PARG inhibitor PDD (Raghunatha et al., 2020) reduced ADE neuronal death in hTRPM2-expressing worms (Fig. 5B and D). These results support that TRPM2 activation is critical for DA neuronal vulnerability. Currently, there is no probe for monitoring the ADPR level and, to explore whether ADPR production plays a role in TRPM2-mediated ADE death, we overexpressed worm NDX-6 (the homologue of human NUDT9), which hydrolyzes ADPR to adenosine monophosphate (AMP) and ribose 5'-phosphate (Fig. 5 A). The results showed that NDX-6 overexpression reduced ADE death in the hTRPM2-expressing worms (Fig. 5B and C), suggesting the importance of ADPR production in TRPM2-mediated ADE neuronal death. Collectively, these results support the notion that the PARP-1/PARG-1/ADPR axis is important for the vulnerability of hTRPM2-expressing ADE neurons in worms.

2.6. The TRPM2-mediated neuronal death pathway is conserved in iPSC-derived DA neurons from a SPD patient

To further determine whether the role TRPM2 plays in mediating DA vulnerability in both *C. elegans* and mice is preserved in PD pathogenesis, we turned to DA neurons differentiated from iPSCs, a well-established cell model for PD research. Using the floor-plate-based midbrain DA neuronal differentiation strategy (Fasano et al., 2010; Ke et al., 2020), we differentiated iPSCs from a sporadic PD (SPD) patient and healthy control into TH-positive DA neurons with ~80% efficiency (Supplementary Fig. 4A-C). Such differentiated iPSC-DA neurons also expressed GIRK2 while calbindin was barely detected (Supplementary Fig. 4B). Both evoked action potentials and voltage-dependent Na^+

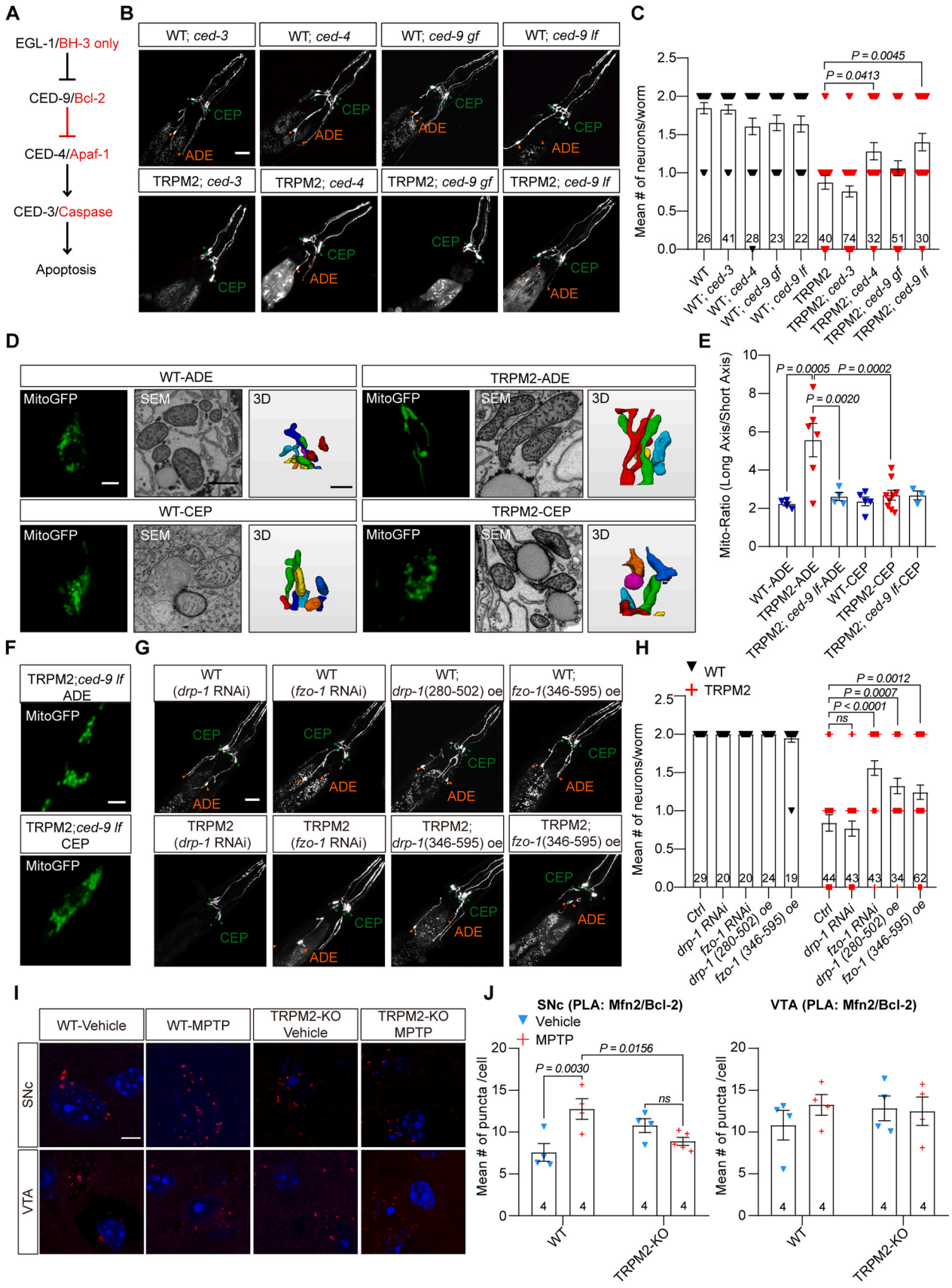

Fig. 4. TRPM2 induces ADE death through FZO-1/CED-9-mediated mitochondrial hyperfusion.

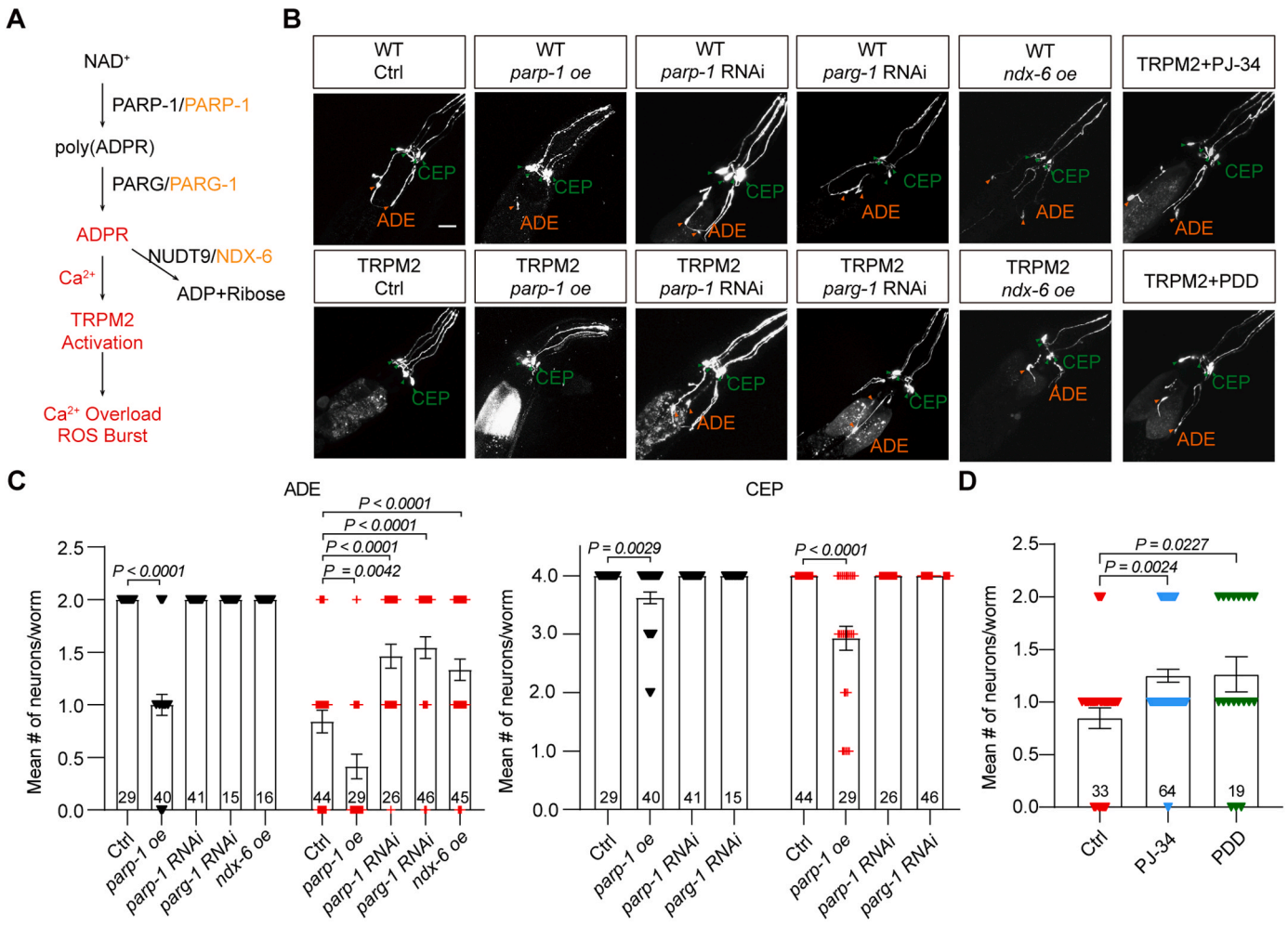

Fig. 5. The PARP-1/PARG-1/ADPR axis-mediated TRPM2 activation induces selective ADE death.

channel currents were detected in the differentiated DA neurons by using whole-cell recording (Supplementary Fig. 4D and E).

Importantly, the viability of SPD iPSC-derived DA neurons was improved by treatment with the TRPM2 inhibitors, ACA or A10 (Fig. 6 A), indicating that TRPM2 function contributes to DA neurons death. We further used a range of inhibitors to determine the role of PARP-1/PARG/ADPR axis in the viability of SPD iPSC-derived DA neurons. As anticipated, inhibition of PARP-1 by treatment with PJ-34 reduced poly(ADPR) formation, whereas inhibition by PARG with PDD increased the poly(ADPR) level (Supplementary Fig. 5 A). Consistently, both PJ-34 and PDD significantly improved the viability of SPD iPSC-derived DA neurons (Fig. 6B-C). In line with the results from our *C. elegans* PD model, we observed Ca^{2+} overload in DA neurons derived from SPD patient-specific iPSC (Supplementary Fig. 5 A and C), which was partially attenuated by treatment with the inhibitors of the PARP-1/PARG/TRPM2 signaling axis, including PJ-34, PDD, ACA or A10 (Supplementary Fig. 5D and E). We also observed mitochondrial hyperfusion in iPSC-derived DA neurons from a SPD patient, but not the healthy control, which was again rescued by treatment with the inhibitors described above (Fig. 6D-E). These results indicate the conserved actions of the PARP-1/PARG/ADPR axis in triggering TRPM2 activation as well as its downstream Ca^{2+} toxicity and mitochondrial hyperfusion in mediating DA neuron death in human SPD cell model.

We further examined whether the TRPM2/FZO-1/CED-9 axis is conserved, and contributes to mitochondrial hyperfusion and MPT, in SPD patient iPSC-derived DA neurons. CED-9 was reported to interact with the coiled-coil domain of FZO-1 (Lu et al., 2011; Rolland et al., 2009). We aligned the *C. elegans* FZO-1 sequence with human Mfn2 and synthesized a polypeptide (PEP) corresponding to the coiled-coil domain (AA391–434) of the human Mfn2 (Fig. 7 A). Using the PLA assay, we showed that PEP treatment strongly inhibited the interaction between the Mfn2 and Bcl-2 in basal condition in SH-SY5Y cells (Fig. 7B and C). MPP^{+}-treated cells exhibited enhanced Bcl-2 and Mfn2 interactions as demonstrated through an increased number of puncta, which was inhibited by treatment with PEP (Fig. 7B-C). This is consistent with our observations on the effects of PEP on rescuing neuronal viability (Fig. 7D), hyperfused mitochondrial morphology (Fig. 6D-E), down-regulating the Mfn2/Bcl-2 interaction (Fig. 6F-G) and intracellular Ca^{2+} in SPD patient iPSC-derived DA neurons (Supplementary Fig. 5D and E). Likewise, inhibition of TRPM2, PARP-1 or PARG activity all significantly suppressed the Mfn2/Bcl-2 interactions in DA neurons from the SPD patient iPSC-derived DA neurons compared to healthy control (Fig. 6F-G). Therefore, our results from a SPD patient iPSC-derived DA neurons are consistent with those in *C. elegans* and mouse models, further supporting the role of Mfn2/Bcl-2-mediated mitochondrial hyperfusion in DA neuronal death across species.

3. Discussion

In this study, we provide clear evidence that TRPM2 plays an important role in mediating the vulnerability of DA neurons using comprehensive cross-model analysis. We have demonstrated that TRPM2 and its novel associated signaling pathways contribute to ROS and Ca^{2+}-dependent mitochondrial hyperfusion, which further results in

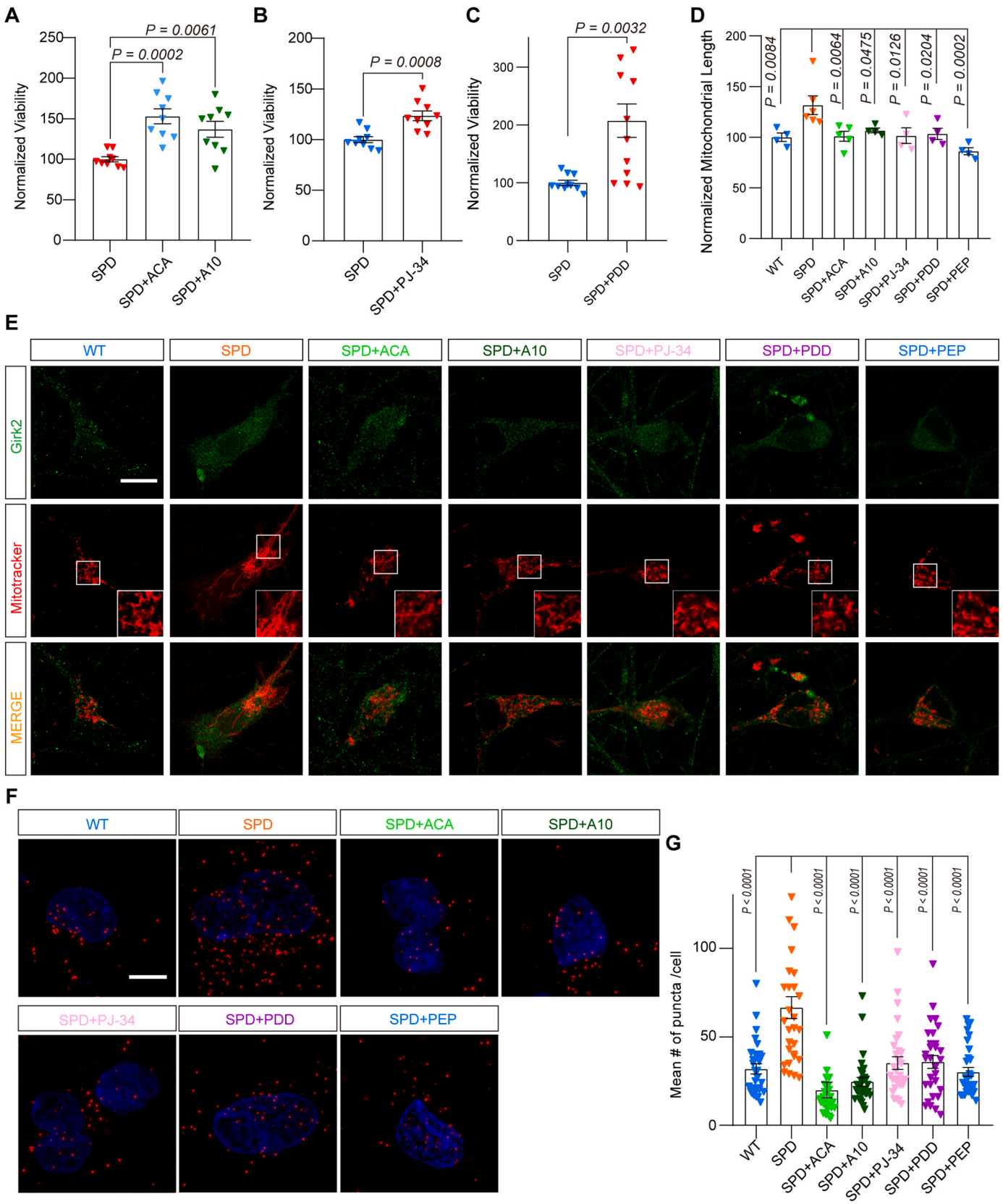

Fig. 6. The TRPM2-mediated neuronal death pathway is conserved in iPSC-derived DA neurons from a SPD patient.

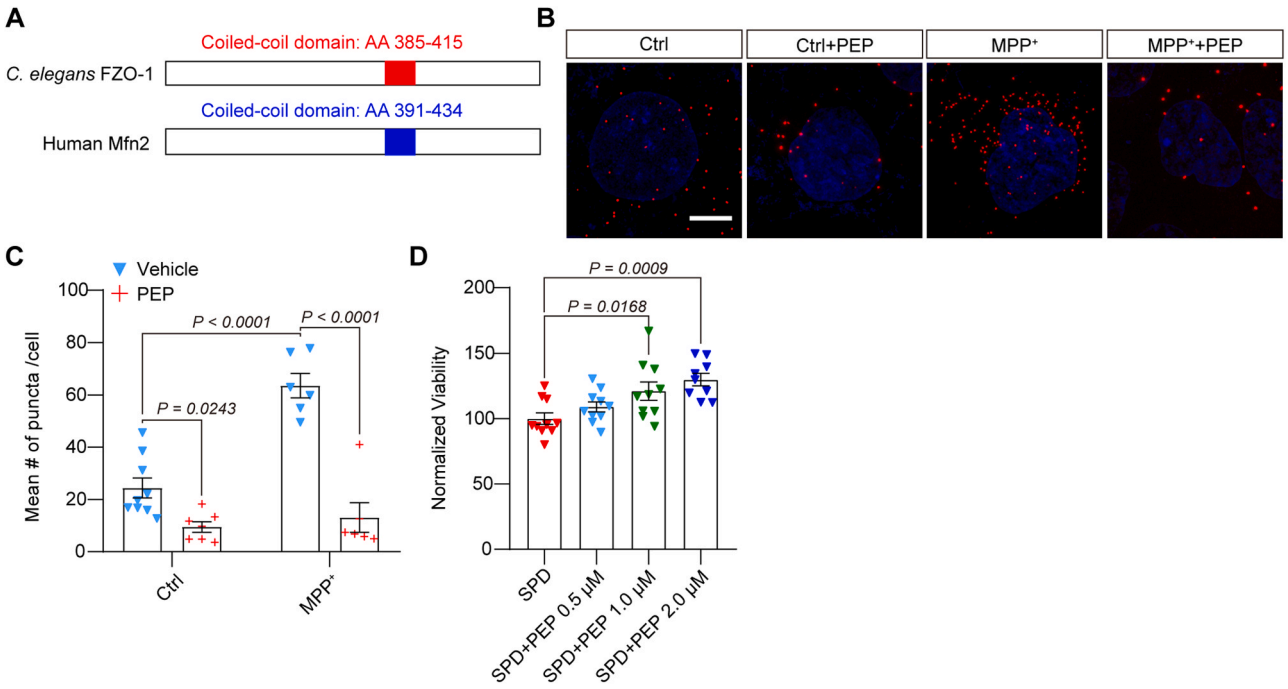

Fig. 7. Synthetic polypeptide antagonizes the interaction between Mfn2 and Bcl-2.

selective DA neuron degeneration in *C. elegans* and mouse models, as well as leading to PD patient iPSC-derived DA neuronal dysfunction. We have also revealed that inhibition of either TRPM2 directly or its associated signaling pathways conservatively improved mitochondrial function, thereby contributing to the survival of vulnerable DA neurons under stress (Fig. 8). These results demonstrate that TRPM2 serves as a critical executor in vulnerable DA neurons by sensing ROS and raising the intracellular Ca^{2+} level to tightly control DA neuronal destination.

TRPM2 as a unique gatekeeper for ROS and Ca^{2+} homeostasis in vulnerable DA neurons across species.

Dopaminergic neurons are classified into different subtypes contributing to their heterogeneity, some of which exhibit vulnerability to external stimuli. A typical example of DA neuron vulnerability is the degeneration of midbrain DA neurons within the SNc region in PD. Postmortem results from PD patients have revealed that the ROS level is significantly higher while the glutathione level is much lower than that of healthy people (Blesa et al., 2015; Ferrer et al., 2011). There is also evidence suggesting that the Ca^{2+} homeostasis plays a critical role in SNc DA neuronal death (Liss and Striessnig, 2019). Benefiting from previously reported single-cell RNA-seq data, we for the first time identified TRPM2, which is activated in response to intracellular ROS and Ca^{2+}, is selectively enriched in vulnerable DA neurons (Fig. 1). Genetic mutations, α-synuclein transgenes, or toxin treatment have previously been reported to result in non-selective DA neuronal death in *C. elegans* (Lakso et al., 2003; Mor et al., 2020; Nagarajan et al., 2014). Through ectopic expression of hTRPM2 channel in the DA neurons of *C. elegans*, we found that there is the heterogeneity of DA neurons in *C. elegans*. In addition, we detected that the levels of both ROS products and Ca^{2+} in the ADE neurons are higher than that in the CEP neurons of hTRPM2-expressing worms during development (Supplementary Fig 3A-B), and treatments with ROS scavenger and Ca^{2+} chelator in TRPM2-expressing worms reduced selective ADE death (Supplementary Fig3C-D), which further supports the theory that both ROS and Ca^{2+} are required for TRPM2-mediated neuronal death. In PD mouse models, our results confirmed that TRPM2-KO protected vulnerable SNc DA neurons from early death (Fig. 3A-B). Moreover, the viability of SPD iPSC-derived DA neurons was significantly improved by treatment with TRPM2 inhibitors (Fig. 6 A). So, it appears highly likely that TRPM2 serves as a redox sensor, and that its selective activation via Ca^{2+}-permeable channels may act as a key player in the manifestation of oxidative stress and Ca^{2+} dyshomeostasis in susceptible DA neurons. Ultimately, this process leads to neuronal degeneration and death as a result of persistent oxidative stress and disrupted Ca^{2+} homeostasis.

Recently, SNc DA neurons have been reported to maintain a state of high-level oxidative stress during autonomous pacemaking, while VTA neurons do not (Guzman et al., 2010). SNc DA neuron-specific L-type Ca^{2+} channels are reported to be involved in autonomous pacemaking activity which results in mitochondrial oxidative stress (Guzman et al., 2010). And the Ca^{2+} buffering capacity has been shown to be significantly lower in SNc DA neurons (Foehring et al., 2009). These vulnerable DA neurons even do not express Ca^{2+}-binding proteins like calbindin as in VTA DA neurons (Mouatt-Prigent et al., 1994). The large axonal arborization, with their high ATP requirements, often seen in SNc may also contribute to this high oxidative stress state (Matsuda et al., 2009). In this way, exposure to additional mild stress may tip the SNc neurons over the edge into degeneration. This evidence sheds light on the vital role of oxidative stress and Ca^{2+} overload in mediating the vulnerability of SNc DA neurons to stress. It takes a long time for DA neurons to degenerate in PD, and the subsequent executors of DA neuronal death due to increased levels of ROS and Ca^{2+} are largely unclear. Our findings suggest that TRPM2 is well positioned to function as the executor that drives the vulnerability of DA neurons upon exposure to oxidative stress and Ca^{2+} dyshomeostasis in these neurons. It is interesting to clarify the signal cascade governing the relationships between autonomous pacemaking activity and TRPM2 activity in SNc DA neurons in the future.

3.1. *CED-4/CED-9 mediates DA neuronal death through MPT*

We observed that the morphology of ADE neurons was accompanied by progressive degeneration of the cell body and processes in the TRPM2-expressing worms, likely related to apoptosis. It is well known that the EGL-1/CED-9/CED-4/CED-3 signaling cascade is a canonical apoptosis pathway (Ellis and Horvitz, 1986). The apoptosis machinery was originally discovered in *C. elegans* and well-conserved in other species (Metzstein et al., 1998). EGL-1, CED-4 and CED-3 have been

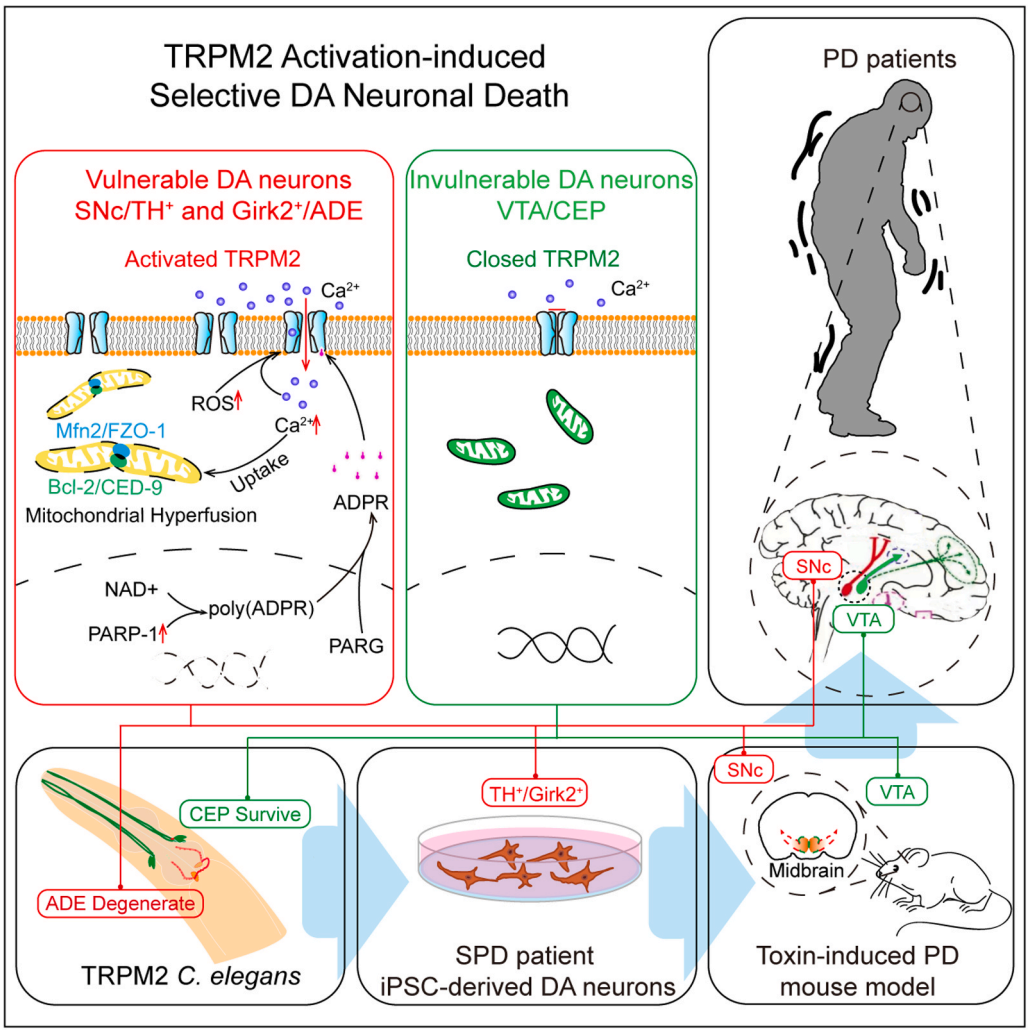

Fig. 8. TRPM2 as a conserved gatekeeper determines the vulnerability of DA neurons by mediating ROS sensing and calcium dyshomeostasis.

reported to promote apoptosis while CED-9 inhibits apoptosis (Metzstein et al., 1998). To our surprise, loss of function of CED-4, but not CED-3 or EGL-1, partially attenuated the ADE neuronal death in the TRPM2-expressing worms. Moreover, loss-of-function rather than gain-of-function of CED-9 strongly suppressed ADE neuronal death, suggesting that a non-classical cell death pathway is mediated by CED-4 and CED-9. In line with our findings, previous studies suggest that both CED-4 and CED-9 regulate cell death through non-canonical apoptosis pathways during development in *C. elegans*. For example, CED-4 plays a critical role in *icd-1* RNAi-induced cell death, and both loss-of-function of CED-3 and gain-of-function of CED-9 failed to prevent this process (Bloss et al., 2003). Our finding presents the first line of evidence to show that a CED-4/CED-9-dependent, non-canonical apoptosis pathway is employed in certain stress conditions. Interestingly, a previous study reported that CED-9 acts as the intracellular interacting target of hepatitis B virus (HBV) protein to induce Ca^{2+} overload, MPT and cell death in *C. elegans* (Geng et al., 2012), but how CED-9 induces MPT is still unknown. In our study, we found that both a *cyn-1* loss-of-function mutation and MPT pore blocker CsA strongly suppressed ADE neuronal death in the TRPM2-expressing worms. MPT opening has been linked to neuronal death by various mechanisms, including excitotoxicity, neurotoxicity, apoptosis and necrosis (Bonora et al., 2022; Perez-Pinzon et al., 2012). Previous studies have reported MPT opening as a consequence of mitochondrial damage resulting in DA neuronal death in PD (Thomas et al., 2012). In mammals, Bcl-2 also plays a central role in regulating MPT during cell apoptosis (Chipuk et al., 2010). Therefore, our findings show that TRPM2 is selectively activated by ROS and Ca^{2+} in ADE neurons, which engage CED-9/CED-4 to trigger MPT and result in ADE neuronal death in the TRPM2-expressing worms.

3.2. *CED-9(Bcl-2)/FZO-1(Mfn-2) mediated mitochondrial hyperfusion is required for TRPM2-dependent vulnerability of DA neurons*

Mitochondrial networks have been reported to undergo severe imbalance upon ROS- or Ca^{2+}-induced stress (Chung et al., 2016; Malpartida et al., 2021). Previous studies suggest that mitochondrial dynamics are related to MPT induction under stressful conditions (Thomas et al., 2012). Emerging evidence indicates that mitochondrial dysfunction is closely associated with the pathogenesis of sporadic and familial PD. Treatment with α-synuclein or pre-formed fibrils (PFFs) was reported to inhibit mitochondrial fusion, resulting in DA neuronal damage (Kamp et al., 2010). In contrast, two iPSC lines- (derived from PD patients with PARK2/Parkin and PINK1 mutations) differentiated DA neurons show a greater proportion of enlarged mitochondria (Chung et al., 2016). Abnormally fused swollen mitochondrial morphology has also been seen in mtDNA-deficient SH-SY5Y cells repopulated with mitochondria from sporadic PD and Alzheimer's Disease (AD) (Trimmer et al., 2000). Moreover, deletion of both Mfn2 and Drp1, which are responsible for mitochondrial fusion and fission respectively, caused DA neuronal death (Berthet et al., 2014; Pham et al., 2012), although it is still debatable whether hyperfission or hyperfusion of mitochondria results in loss of DA neurons in PD. Surprisingly, by using fluorescent

probes and 3D-electronic microscopy, we found that hyperfused mitochondria are increased in the hTRPM2-expressing worms but not in the WT worms (Fig. 4D-E). Moreover, knockdown of FZO-1 dramatically reduced ADE neuronal death in the TRPM2-expressing worms (Fig. 4G-H), suggesting that TRPM2 promotes FZO-1-mediated hyperfusion. As expected, we observed that mitochondrial hyperfusion in the hTRPM2-expressing worms was inhibited by expressing loss of function of CED-9 or the CED-9 binding domain of FZO-1 (Fig. 4F-H), supporting a key role of CED-9 in promoting mitochondrial fusion, dependent on the CED-4 and FZO-1 complex (Lu et al., 2011). In line with our finding, previous studies observed that in *C. elegans,* CED-9 acts as a molecular switch to regulate mitochondrial fission/fusion balance by interacting with FZO-1 or DRP-1 under certain conditions (Lu et al., 2011; Rolland et al., 2009), and that CED-9 overexpression promoted mitochondrial fusion in human cell lines (Delivani et al., 2006). Conversely, others argue that CED-9 is not involved in controlling mitochondrial dynamics in *C. elegans* (Breckenridge et al., 2009).

Consistent with the findings in *C. elegans*, we observed that DA neurons differentiated from iPSC derived from SPD patient exhibited mitochondrial hyperfusion, which was restored by inhibition of the PARP-1/PARG/TRPM2 and, more importantly, by treatment with the polypeptide disrupting the Bcl-2/Mfn2 interaction (Fig. 6D-E). We also found that the Bcl-2/Mfn2 interaction was increased in the SNc region in MPTP-induced PD mice (Fig. 4I-J). Furthermore, TRPM2-KO attenuated the Bcl-2/Mfn2 interaction in vulnerable SNc DA neurons in PD mice (Fig. 4I-J). There is evidence that Ca^{2+} oscillation is required for increased mitochondrial fusion in the heart (Eisner et al., 2017). However, it is unclear how TRPM2 activation triggers the interaction of CED-9 (Bcl-2) with FZO-1 (Mfn2) in vulnerable DA neurons. TRPM2 is located in the plasma membranes and membranes of mitochondria and lysosomes, all of which play key roles in controlling intracellular Ca^{2+} homeostasis in a variety of cells (Malko and Jiang, 2020). It is interesting to investigate how TRPM2-mediated increase in the intracellular Ca^{2+} level triggers the CED-9(Bcl-2)/FZO-1(Mfn2) interaction in DA neurons in the future. As we showed in worms and mice, our results from using iPSC-differentiated human DA neurons support a similar mechanism is critically involved in determining the vulnerability of human neuronal death and, nonetheless, further studies are required to strengthen this finding.

3.3. *TRPM2 mediates the vulnerability of DA neurons via the PARP-1/PARG/ADPR axis*

As the major endogenous ligand of TRPM2, ADPR is mainly produced by coordinated actions of PARP-1 and PARG, mechanisms important for repairing DNA damage. Our electrophysiological results showed that ADPR-induced hTRPM2 channel currents did not differ between ADE and CEP neurons in the hTRPM2-expressing worms (Supplementary Fig 2H-I). Genetic knockdown of *parp-1* and *parg-1* expression in worms or treatment with PJ-34 and PDD dramatically suppressed ADE neuron degeneration in the hTRPM2-expressing worms. Conversely, overexpression of *parp-1* in DA neurons not only led to ADE neuronal death in both WT and hTRPM2-expressing worms, but also induced degeneration of CEP neurons in hTRPM2-expressing worms. These results clearly indicate that PARP-1 is responsible for TRPM2-mediated ADE death in the TRPM2-expressing worms. There is evidence that PARP-1 plays a critical role in PD pathogenesis by regulating poly(ADPR)-induced aggregation of α-synuclein or through apoptosis-inducing factor (AIF)/migration inhibitory factor (MIF)-dependent chromatinolysis (Kam et al., 2018; Wang et al., 2016; Wang et al., 2011). Our findings not only support that PARP-1 is crucial for SNc DA neurodegeneration in PD but also reveal a novel mechanism for PARP-1 in mediating the vulnerability of DA neurons. Future studies are necessary to better understand the potential relationships between poly (ADPR)-induced α-synuclein aggregation and TRPM2 in regulating the vulnerability of DA neurons in PD.

While pathological α-synuclein PFF activates PARP-1 and causes SNc DA neural death via parthanatos in PD (Kam et al., 2018; Wang et al., 2016; Wang et al., 2011), the role of PARG in PD remains poorly defined. Our results showed that inhibition of PARG suppressed loss of ADE neurons in the TRPM2-expressing worms (Fig. 5B-D) and dysfunction of SPD iPSC-derived DA neurons (Fig. 6 and Supplementary Fig 5). In addition, overexpression of NDX-6 that catalyzed ADPR hydrolysis significantly reduced loss of ADE neurons in the hTRPM2-expressing worms (Fig. 5B-C). These results provide consistent evidence to show for the first time that the PARP-1/PARG-1/ADPR signaling axis is required for TRPM2-mediated vulnerability of DA neurons. Finally, we noted that the TRPM2 channel is functionally expressed in worm ADE and CEP neurons at a similar level, based on our electrophysiological results (Supplementary Fig 2H-I), the TRPM2 mRNA expression level was higher in vulnerable SNc DA neurons in mammals (Fig. 1 and Supplementary Fig 1), further supporting the notion that TRPM2 is a key mechanism for discriminately causing DA neuronal death.

In conclusion, we have revealed that TRPM2 acts as a novel mediator or amplifier to mediate the vulnerability of DA neurons. By sensing the intracellular ROS and Ca^{2+}, TRPM2 results in mitochondrial hyperfusion by enhancing the Bcl-2/Mfn2 interaction and MPT that ultimately leads to DA neuron degeneration during PD pathogenesis.

(A) UMAP of iPSC-differentiated DA neurons. **(B)** Percentage of different neuron clusters in control and rotenone-treated groups. **(C)** UMAP of KCNJ6 expression. **(D)** UMAP of CALB1expression. **(E)** The expression abundance of human TRPM2, TRPC6 and TRPA1 in different neuron clusters from the "Ctrl" group. **(F)** The expression of TRPM2 in neurons from single-cell transcriptomic data of PD patients' SNc. Student's t-test. **(G)** Scatterplot depicting the correlation between age and TRPM2 expression level in SNc neurons of PD patients from the upper panel. **(H)** UMAP showing 10 transcriptionally distinct subpopulations based on snRNA-seq of human SNc DA neurons nucleus. The highly vulnerable DA neuron cluster "SOX6_AGTR1" is marked in pink. **(I-K)** Scatterplot and boxplot showing the expression of KCNJ6 (GIRK2), Calbindin (CALB1) and TRPM2. **(L)** Representative fluorescent RNA-scope images showing the expression of TRPM2 (red puncta) in TH^{+}(green) neurons from the ventral tier of SNc and VTA region in mice at 10- and 40- weeks stage. Blue is DAPI staining. Scale bar = 20 μm. **(M)** Quantification of TRPM2 mRNA based on the number of red puncta per TH-positive neurons. Two-way ANOVA with Holm-Sidak's multiple comparisons test (n = 3). The average number of puncta of each mouse was calculated from 6 spaced-out brain sections (one slice every six of spanning the whole SNc from bregma −2.7 mm to −4.04 mm from front to back in space) .

(A) Representative confocal images showing ADE and CEP DA neurons in WT and hTRPM2-expressing worms on adult day 1, day 4 and day 7. Scale bar = 20 μm. **(B)** Quantification of ADE and CEP DA neurons in WT and hTRPM2-expressing worms. Error bars represent mean ± s.e.m. P values are from Two-way ANOVA with Holm-Sidak's multiple comparisons test. **(C)** Diagram illustrating the membrane arrangement of the hTRPM2 channel subunit. The loss-of-function E960Q mutation is within the pore region between transmembrane (TM) segments S5 and S6. The loss-of-function R1433A mutation is located in the ADPR-binding domain in the C-terminus. **(D)** Representative confocal images showing ADE and CEP DA neurons in worms expressing indicated hTRPM2 mutants. **(E)** Quantification of ADE DA neurons in worms expressing human WT TRPM2, TRPM2(E960Q) and TRPM2(R1433A) mutants. Error bars represent mean ± s.e.m. P values are from Dunnett's multiple comparisons test following one-way ANOVA.

(A) DA neurons in WT and TRPM2-KO mice after treatment with MPTP or vehicle. Confocal images showing the expression of TRPM2 in TH-positive DA neurons in the SNc and VTA regions. Scale bar = 50 μm; scale bar for zoomed-in view = 20 μm. **(B)** Quantification of TH-positive neurons in the SNc region. Scale bars = 50 μm or 200 μm. Two-way ANOVA with Holm-Sidak's multiple comparisons test. Data expressed as mean ± s.e.m. n = 6–9. **(C)** Schematic summarizing rotenone (Rot)-

induced PD mouse model and experimental designs. **(D)** TRPM2-KO reduced APO-induced rotation behaviors in the first and second weeks after treatment with Rot. Data expressed as mean ± s.e.m. n = 9–13. Two-way ANOVA with Holm-Sidak's multiple comparison test. **(E)** Right, results of Rot-treated PD mice on the rotarod test. Data expressed as mean ± s.e.m. n = 9–13. Two-way ANOVA with Holm-Sidak's multiple comparisons test. **(F)** Representative confocal images showing TH-immunoreactive (TH^+) fibers in the striatum from 4 different groups of mice treated with Rot. Scale Bar for zoomed region = 20 μm. Scale Bar of the central images = 1000 μm. **(G)** Quantification of TH^+ fibers on the lesioned or unlesioned side of the striatum. Data expressed as mean ± s.e.m. n = 5, 7. Two-way ANOVA with Holm-Sidak's multiple comparison test.

(A) Key regulators of apoptosis in *C. elegans* with human homologues in red. **(B)** Representative confocal images showing WT and hTRPM2-expressing worms carrying *ced-3 (n717), ced-4 (n1162), ced-9 (n1950, gain-of-function)* and *ced-9 (n2812, loss-of-function)* mutations. Scale bar = 20 μm. **(C)** Quantification of ADE neurons in the panel B experiment. One-way ANOVA with Dunnett's multiple comparisons test. **(D)** Representative confocal images, SEM images and SEM 3D-reconstruction images showing mitochondria in ADE and CEP neurons in WT and hTRPM2-expressing worms. Confocal images: scale bar = 2 μm. SEM: scale bar = 500 nm. 3D SEM: scale bar = 1 μm. **(E)** Statistical analysis of the ratio of longer axis/short axis of mitochondria based on confocal images. One-way ANOVA with Dunnett's multiple comparisons test. **(F)** Confocal images showing the effect of *ced-9 loss-of-function* mutation on mitochondrial morphology in ADE and CEP neurons in WT and hTRPM2-expressing worms. Scale bar = 2 μm. **(G)** Representative confocal images showing the effects of *drp-1* RNAi, *fzo-1* RNAi, *drp-1 (280−502)* overexpression and *fzo-1 (346−595)* overexpression on ADE and CEP neurons in WT and hTRPM2-expressing worms. Scale bar = 20 μm. **(H)** Quantification of ADE neurons in the panel G experiment. Two-way ANOVA with Holm-Sidak's multiple comparisons test. **(I)** Positive PLA signals (red spots) show the interaction of Bcl-2 and Mfn2 in WT and TRPM2- knockout mice after treatment of MPTP or vehicle. Scale bar = 5 μm. **(J)** Quantification of the number of PLA spots indicating the Mfn2/Bcl-2 interaction in the SNc and VTA regions. Data expressed as mean ± s.e.m. n = 4, 5. Two-way ANOVA with Holm-Sidak's multiple comparisons test.

(A) A schematic showing the key enzymes involved in ADPR synthesis and metabolism. The TRPM2 channel is activated by ADPR and Ca^{2+}. **(B)** Representative confocal images showing WT and hTRPM2-expressing worms with *parp-1* overexpression, *parp-1* knockdown, *parg-1* knockdown, ndx-6 overexpression, and treated with PJ-34 or PDD. Scale bar = 20 μm. **(C)** Quantification of ADE and CEP neurons in the panel B experiment. Two-way ANOVA with Holm-Sidak's multiple comparison test. **(D)** Quantification of ADE neurons in the panel B experiment (PJ-34 and PDD treatment). One-way ANOVA with Dunnett's multiple comparison test.

(A) Summary of the effects of treatment with ACA (0.5 μM), A10 (0.6 μM) on the viability of iPSC-derived DA neurons from a SPD patient. Data expressed as mean ± s.e.m. P values are from one-way ANOVA with Holm-Sidak's multiple comparison test. **(B)** Summary of the effect of treatment with PJ-34 (2 μM) on the viability of iPSC-derived DA neurons from a SPD patient. Data expressed as mean ± s.e.m. P value is from Student's t-test. **(C)** Summary of the effect of treatment with PDD (1 μM) on the viability of iPSC-derived DA neurons from a SPD patient. Data expressed as mean ± s.e.m. P value is from Student's t test. **(D)** Statistical analysis of the relative length of mitochondria branches. Data expressed as mean ± s.e.m.; P values are from One-way ANOVA with Dunnett's multiple comparison test. **(E)** Representative confocal images showing mitochondrial networks in SPD patient iPSC-derived DA neurons treated with PJ-34, PDD, A10, ACA or PEP. Scale bar = 20 μm. **(F)** Positive PLA signals (red spots) showing the interaction of Bcl-2 and Mfn2 in human iPSC-derived DA neurons determined via PLA assay. Scale bar = 5 μm. **(G)** Quantification of the number of PLA spots indicating the Mfn2/Bcl-2 interaction in human iPSC-derived DA neurons. Data expressed as mean ± s.e.m. One-way ANOVA with Holm-Sidak's multiple comparison test.

(A) Schematic showing the localization of the coiled-coli domains in worm FZO-1 and human Mfn2. **(B)** Representative confocal images showing that PEP (10 μM) inhibited the interaction of Bcl-2 and Mfn2 in SH-SY5Y cells after treatment with MPP^+ or vehicle. The red fluorescence puncta indicate the interaction of Mfn2 and Bcl-2 detected by PLA. Scale bar = 5 μm. **(C)** Quantification of red puncta in panel **B**. Data expressed as mean ± s.e.m. n = 6–9. Two-way ANOVA with Holm-Sidak's multiple comparison test. **(D)** The viability of iPSC-derived DA neurons from a SPD patient and those treated with PEP Data expressed as mean ± s.e.m. P values are from one-way ANOVA with Holm-Sidak's multiple comparison test.

Graphical representation of the key findings. TRPM2 channel is preferentially activated in vulnerable DA neuron groups in different models, and activated by the PARP-1/PARG/ADPR axis in response to stress, leading to Ca^{2+} overload, oxidative stress, interaction of Mfn2/Bcl-2 (FZO-1/CED-9 in *C. elegans)* and mitochondrial hyperfusion, and ultimately vulnerability of DA neurons.

4. Materials and methods

4.1. Key resources table

Reagent/Resource	Reference or Source	Identifier or Catalog Number
Experimental Models		
C57BL/6 J (*M. musculus*)	Jackson Lab	B6.129P2Gpr37tm1Dgen/J
C57BL/6 J-TRPM2-KO (*M. musculus*)	Zou et al. (2013)	
N2	CGC	ST348
kanIs15[Pdat-1::sl2::DsRed2b+Punc-122::GFP]	This study	ST1964
kanIs16[Pdat-1::hTRPM2::sl2::DsRed+Punc-122::GFP]	This study	ST1963
kanIs17 [Pdat-1::hTRPM2 (E960Q)::sl2::DsRed+Punc-122::GFP]	This study	ST2285
kanIs18 [Pdat-1::hTRPM2 (R1433A)::sl2::DsRed+Punc-122::GFP]	This study	ST2283
kanIs15; kanEx773[Pdat-1::parp-1 + Plin-44::mCherry]	This study	ST3243
kanIs16; kanEx773[Pdat-1::parp-1 + Plin-44::mCherry]	This study	ST3244
kanIs15; kanEx885[Phsp-16.2::parp-1 RNAi-sense+ Phsp-16.2::parp-1 RNAi-sense+Plin-44::mCherry	This study	ST3102
kanIs16; kanEx885[Phsp-16.2::parp-1 RNAi-sense+ Phsp-16.2::parp-1 RNAi-antisense+Plin-44::mCherry]	This study	ST3103
kanIs15; kanEx886[Phsp-16.2::parg-1 RNAi-sense+ Phsp-16.2::parg-1 RNAi-antisense+Plin-44::mCherry]	This study	ST3104
kanIs16; kanEx886[Phsp-16.2::parg-1 RNAi-	This study	ST3105

(*continued on next page*)

(*continued*)

Reagent/Resource	Reference or Source	Identifier or Catalog Number
sense+ Phsp-16.2::parg-1 RNAi-antisense+Plin-44::mCherry]		
kanIs15; kanEx721[Pdat-1::ndx-6 +Plin-44:: mCherry]	This study	ST3054
kanIs16; kanEx721[Pdat-1::ndx-6 +Plin-44:: mCherry]	This study	ST3055
cyn-1 (tm4171) V	CGC	ST3263
kanIs15; cyn-1 (tm4171) V	This study	ST2936
kanIs16; cyn-1 (tm4171) V	This study	ST2937
ced-3 (n717) IV	CGC	MT1522
kanIs15; ced-3 (n717) IV	This study	ST1956
kanIs16; ced-3 (n717) IV	This study	ST2304
ced-4 (n1162) III	CGC	MT2547
kanIs15; ced-4 (n1162) III	This study	ST1951
kanIs16; ced-4 (n1162) III	This study	ST1950
ced-9 (n2812) III /hT2	CGC	CU3693
kanIs15; ced-9 (n2812) III /hT2	This study	ST2076
kanIs16; ced-9 (n2812) III /hT2	This study	ST2078
ced-9 (n1950) III	CGC	MT4770
kanIs15; ced-9 (n1950) III	This study	ST2312
kanIs16; ced-9 (n1950) III	This study	ST2318
egl-1 (n1084n3082) V	CGC	MT8735
kanIs16; egl-1 (n1084n3082) V	This study	ST231
N2; kanEx646[Pdat-1:: mitogfp+Plin-44:: mCherry]	This study	ST3035
kanIs19 [Pdat-1::TRPM2:: sl2::mitogfp+Plin-44:: mCherry]	This study	ST3040
kanIs15; kanEx813[Pdat-1::miniSOG+Plin-44:: mCherry]	This study	ST2848
kanIs16; kanEx813[Pdat-1::miniSOG+Plin-44:: mCherry]	This study	ST2849
kanIs15; kanEx844[Phsp-16.2::drp-1 RNAi-sense+ Phsp-16.2::drp-1 RNAi-antisense+Plin-44::mCherry]	This study	ST2776
kanIs16; kanEx844[Phsp-16.2::drp-1 RNAi-sense+ Phsp-16.2::drp-1 RNAi-antisense+Plin-44::mCherry]	This study	ST2777
kanIs15; kanEx845[Phsp-16.2::fzo-1 RNAi-sense+ Phsp-16.2::fzo-1 RNAi-antisense+Plin-44::mCherry]	This study	ST3146
kanIs16; kanEx845[Phsp-16.2::fzo-1 RNAi-sense+ Phsp-16.2::fzo-1 RNAi-antisense+Plin-44::mCherry]	This study	ST3147
kanIs15; kanEx920[Pdat-1::drp-1 (280–502)+ Plin-44::mCherry]	This study	ST2929
kanIs16; kanEx920[Pdat-1::drp-1 (280–502)+ Plin-44::mCherry]	This study	ST2930
kanIs15; kanEx921[Pdat-1::fzo-1 (346–595)+ Plin-44::mCherry]	This study	ST2931
kanIs16; [parp-1-GFP11x7]; Ex[Pdat-1:: GFP 1–10]	This study	*ST3103*

(*continued on next column*)

(*continued*)

Reagent/Resource	Reference or Source	Identifier or Catalog Number
Antibodies		
Mouse anti Tyrosine Hydroxylase (TH)	Millipore	Cat # MAB318
Rabbit anti MAP2	Proteintech	Cat # 1749001–1–1AP
Goat anti Girk2	Abcam	Cat # Ab65096
Rabbit anti PARP1	Cell Signaling Technology	Cat # 9542
Mouse anti poly(ADPR)	Enzo	Cat # ALX-804–220
Mouse anti β-tubulin	Abclonal	Cat # WH119842
Rabbit anti TRPM2	Abcam	Cat # Ab96785
Mouse anti Bcl-2	Santa Cruz	Cat # sc-7382
Rabbit anti Mfn2	Abcam	Cat # Ab124773
Anti-Oct4	Abcam	Cat # Ab19857
Anti-Tra-1–60	Abcam	Cat # Ab19288
Anti-Nanog	Abcam	Cat # Ab109250
Anti-SOX-2	Abcam	Cat # Ab97959
Chemicals, Enzymes and other reagents		
DAPI	SouthernBid	Cat # 0100–02
A10 ((E)− 2-(3-(4-(Pyridin-3-yl)phenyl) acrylamido)benzoic Acid)	Provided by Liangren Zhang's Lab, State Key Laboratory of Natural and Biomimetic Drugs, School of Pharmaceutical Sciences, Peking University	
ACA (N-(p-amylcinnamoyl) anthranilic acid)	MCE	Cat # 110683–10–8
PJ-34 hydrochloride	MCE	Cat # HY-13688
PDD 00017273	MCE	Cat # HY-108360
PEP	DENTRIPHARM	Cat # 200430–102
Rotenone	Sigma	Cat # R8875
MPTP	Sigma	Cat # M0896
MPP^+	Sigma	Cat # D048
Apomorphine hydrochloride	National Institutes for Food and Drug Control	Cat # LNBH-4GT3
BAPTA-AM	MCE	Cat # HY-100545
ADPR	Sigma	Cat # A0752
NAC (N- Acetylcysteine)	MCE	Cat # HY-B0215
Software *Include version where applicable*		
Fiji	https://fiji.sc/	
Graphpad Prism	https://www.graphpad.com/	
Other		
Duolink-PLA	Sigma	Cat # DUO92008
Cell Titer Glo Assay	Promega	Cat # PR-G7571
In-Fusion HD Cloning Kit	Takara	Cat # 639649
Fluo-4 AM	ThermoFisher	Cat # F14201
Mitotracker	ThermoFisher	Cat # M22425

5. Methods and Protocols

5.1. C. elegans

5.1.1. Maintenance of C. elegans

Worms were cultured under standard conditions on nematode growth medium (NGM) plates at 20 °C, fed with OP50 as previously described (Corsi et al., 2015). Strains used in this study were listed in Reagents and Tools table.

5.2. Generation of C. elegans strains

The coding sequence of human TRPM2 was cloned into the plasmid *Pdat-1::sl2::DsRed2b* under the control of *Pdat-1* promoter, and the *sl2* sequence and DsRed2b were retained as a positive mark of hTRPM2 expression. For hTRPM2 and WT (with DsRed2b specifically expressed

in DA neurons only) transgenic *C. elegans* construction, the plasmids (50 ng/μL) together with 10 ng/μL co-marker *Punc-122-GFP* were injected into the gonad of young adult worm. The offspring with DsRed2b expression were isolated for integrated strains construction. Arrays were integrated into the genome with trimethylpsoralen/ultraviolet (TMP/UV) mutagenesis. Extrachromosomal array transgenic animals were made by gonad injection of constructed plasmids at 40–50 ng/μL with 10 ng/μL co-injection marker (*Plin-44-mCherry*). We selected WT and hTRPM2-expressing worms that express similar fluorescent intensities of DsRed2b for experiments.

5.3. Neurodegeneration Assay

Animals were immobilized on 2% agarose pads in M9 buffer with 12 mM levamisole (TCI, T1215). Representative images were obtained on Olympus FV1000 confocal microscope at 60x magnification, the heads of the worms were observed and captured for better imaging of ADE and CEP neurons using a 546 nm excitation laser, and Z stacks were processed with FV10-ASW 4.2 Viewer. ADE and CEP neurons with visible soma and continuent process were counted as survival neurons and each worm were checked by two independent researchers.

5.4. Quantitation of neruonal Calcium and ROS level

To measure calcium and ROS level via genetic GCaMP3 and Hyper fluorescent probe respectively, the coding sequence of probes were cloned into the plasmids under the control of *Pdat-1* promoter. Then the probe plasmids and the comaker (*Plin-44-mCherry)* were injected into the gonad of young adult worms. We acquired images using the confocal microscopy with 488 nm and 546 nm excitation using a 60x objectives (Olympus, FV1000). To quantify calcium and ROS level (F_{488}), we measured average fluorescence of neuronal cell bodies. The baseline fluorescence $F_{488\text{-background}}$ was obtained by averaging fluorescence of head epidermis. The normalized calcium and ROS level was calculated as (F_{488}-$F_{488\text{-background}}$)/ ($F_{546}$-$F_{546\text{-background}}$).

5.5. Electrophysiology

Day 2 adult worms were glued on the surface of Sylgard-coated coverslips using cyanoacrylate-based glue. A dorsolateral incision was made using sharp glass pipettes to expose the head-located dopamine neurons. Whole-cell current recordings were performed on a fluorescent microscope (Olympus, BX51W1) using an EPC-10 amplifier and Patchmaster software (HEKA). The extracellular solution (ECS) contained 145 mM NaCl, 2.5 mM KCl, 5 mM $CaCl_2$, 1 mM $MgCl_2$, 20 mM glucose, pH 7.3. The intracellular solution (ICS) contained 145 mM K-gluconate, 2.5 mM KCl, 0.25 mM $CaCl_2$, 5 mM $MgCl_2$, 5 mM EGTA, 10 mM HEPES, 10 mM glucose, 5 mM Na2ATP and 0.5 mM NaGTP, pH 7.2. The membrane potential was held at − 70 mV. 1 mM ADPR and 10 μM CaCl2 were added to ICS when tested for ADPR and Ca^{2+} coordinated activation of TRPM2 and 20 μM ACA was added to the ECS. The data were processed with Igor software (WaveMetrics).

5.6. Neuronal RNAi

As the neurons of *C. elegans* are not susceptible to systematic feeding RNAi (Calixto et al., 2010; Firnhaber and Hammarlund, 2013), we conduct injection RNAi with mixed gene fragments in sense and antisense orientation under *Phsp-16.2* promoter, for its time-specific initiation and neuronal RNAi effect (Esposito et al., 2007; Hamakawa and Hirotsu, 2017; Tavernarakis et al., 2000). The sense and antisense fragments of the target gene were injected at 40 ng/μL each with 10 ng/μL co-injection marker *(Plin-44-mCherry)*. Young L4 worms were heat-shocked at 35 °C for 30 min every day and then incubated at 20 °C until day 7 in adulthood for neuronal counting.

5.7. Drug treatment

Detailed information about the antibodies, drugs and commercial kit used in this study were listed in Reagents and Tools table. All drugs were dissolved at high concentration as stock solutions. PJ-34 (Sigma, P4365), PDD (Adipogen Life Sciences AG-CR1–3646-M005), NAC (Sigma, A9165), BAPTA-AM (Sigma, A1076) were dissolved in DMSO or H2O to make 10 mM stock solutions respectively. Drugs were added to the bacterial lawn of seeded NGM plates, and the drug NGM plates were allowed to dry for several hours. For drug treatment, L4 worms were transferred to the drug plates. Considering the drug effect decline, worms were transferred to other fresh-made drug plates every 2 days.

5.8. SEM and 3D reconstruction

The SEM preparation of worms was conducted as previously described (Shu et al., 2011) with some modifications. To better determine the location of ADE and CEP neurons, every worm was observed with a confocal microscope (Olympus FV1000) first to determine the distance from the anterior to the cell body of the target neurons according to the DsRed2b fluorescence. Worms were then removed into PCR tubes for SEM sample preparation. Worms were fixed with 2% PFA and 1% glutaraldehyde in pH 7.4 0.1 M sodium cacodylate (CAS) buffer for 2 h, and the cuticle was sharply cut to allow diffusion of 4% glutaraldehyde fixing buffer for better fixing overnight. Worms were washed with CAS buffer 3 times and removed into diaminobenzidine (DAB) buffer to allow the diffusion of DAB into the head for 480 nm intense light photooxidation together with bubbled oxygen for 5 min. Worms were washed 3 times with CAS buffer and post-fixed in 2% osmium tetroxide in 0.1 M CAS buffer for 30 min on ice, and washed three times with ddH2O. 1% aqueous uranyl acetate was used to stain worms for 1 h at 4 °C, followed by washing with ddH2O 3 times again. The samples were dehydrated in a graded ethanol series (30%, 50%, 70%, 90%, 100%) for 30 min in each step. Worms were washed with a 1:1 mixture of acetone and methanol, pure acetone twice, respectively. The samples were soaked in mixture of 3:7, 7:3, 1:0 resin and acetone in order for 12 h, 24 h and 48 h, respectively. Finally, the samples were put in a vacuum oven at 65 °C for 48 hr. The position of worms was adjusted parallel to the sample well to locate the neurons. The resin samples were cut at micrometer grade to the desired area according to the recorded distance before, and images of each thin section (10 nm) were collected on Nova Nano 450 (Thermo, FEI). The serial images were aligned and reconstructed using Amira software (Thermo Fisher Scientific). Finally, manual segmentation was performed to label the boundaries of photooxidated DAB-stained mitochondria for 3D reconstruction.

5.9. Mice

The Trpm2 − /− male mice (8–10 weeks of age, 22–25 g) were bred in Zhejiang University after being introduced from University of Leeds, where the transgenic mice were generated (Zou et al., 2013). They were group-housed in a controlled environment (21 ± 2 °C, 12-hr light/dark cycle) with free access to food and water. The ethical standards of the experiments were in accordance with the guidelines of the institutional Animal Care and Use Committee of Zhejiang University. Efforts were made to minimize the number of animals used and their discomfort.

5.10. MPTP-induced mouse model of PD

Mice were randomly divided into vehicle and MPTP (1-methyl-4-phenyl-1,2,3,6-tetrahydropyridine) groups. The MPTP group was intraperitoneally injected with 25 mg/kg/day of MPTP for five consecutive days as described previously (Jackson-Lewis and Przedborski, 2007; Wei et al., 2020), whereas the control mice were injected with equal volume of a standard suspension vehicle (0.9% NaCl, w/v) (Jackson-Lewis and Przedborski, 2007; Tatton and Kish, 1997). Mice

were sacrificed 6 days following the last injection, upon completion of rotarod tests. The animals were perfused with 4% paraformaldehyde in 0.1 M phosphate buffer (pH 7.4) and coronal cryo-sections at a thickness of 20 μm were prepared for immunofluorescence staining.

5.11. Stereotaxic surgery (Rotenone-induced mouse model of PD

We used animal surgery procedures as described in detail in our previous studies with minor modifications (Fang et al., 2021). In short, mice were deeply anesthetized with 1.5% pelltobarbitalum natricum (6 ml/kg, i.p.) and placed in a stereotaxic frame (Refworld, Shenzhen, China). A total of 2.5 μg rotenone (R8875, Sigma-Aldrich, St. Louis, MO, USA) (1 μg/μL, dissolved in 5%DMSO+5%cremophor+90%vehicle) was infused into the left SNc (Bregma point: lateral (L)= 1.2 mm; antero-posterior(AP)= −3.1 mm; and dorso-ventral (DV)= 4.5 mm) and MFB (Bregma point: lateral (L)= 1.1 mm; antero-posterior(AP)= −1.2 mm; and dorso-ventral (DV)= 5.1 mm) at a flow rate of 1 μL/min by a micro-infusion apparatus (Refworld, Shenzhen, China). Sham-operated mice received an equal volume of the vehicle only.

5.12. Tyrosine hydroxylase (TH) immunofluorescence staining

The midbrain SNc and striatum were cut coronally on a frozen sliding microtome (Leica, Wetzlar, Germany) at 20 μm. Slices were collected and processed for TH immunofluorescence staining. In brief, brain slices were blocked in 3% BSA with 1% TBST for 2 hr at room temperature. After the blocking step, brain slices were incubated overnight with anti-tyrosine hydroxylase antibody (clone LNC1; MAB318, Sigma) (1:5000) at 4 °C with 1% BSA in 0.3% PBST. On next day, brain slices were washed in PBS three times, for 5 min each time, and then incubated in fluorescent-conjugated goat antibody to mouse IgG-H&L for 2 hr. We analyzed multiple slices (one slice every four of spanning the whole SNc from bregma −2.7 mm to −4.04 mm) for TH staining neuron counting. Fluorescence images were captured using an Olympus VS120 microscope, with10X and 20X objectives. Subsequent quantification and analysis of the images were performed in CellSens Dimension.

5.13. Rotarod test

Mouse motor coordination was evaluated using a rotarod apparatus (Bieri et al., 2019). Mice were trained on 3 consecutive days for 300 s at a constant speed of 5 rpm/min to acclimate them to the rotarod apparatus. For the testing, the rotarod test was conducted at a uniformly accelerating speed from 5 to 30 r/min in 300 s, and the latency to fall was recorded for 3 trials, and the rod and chambers were wiped with 70% ethanol between trials.

5.14. Apomorphine-induced rotations

The animals were habituated to the environment for 30 min. Then, the mice were tested in response to apomorphine (0.5 mg/kg; i.p.) initially on the 7th and 14th day. Consistent with our previous standard (Zhou et al., 2019), Rotations (360°, in short axis) were counted. The recording continued for 60 min

5.15. iPSC

5.15.1. DA neuron differentiation

Floor plate (FP)-cell-based DA neuron induction was performed as previously described (Fedele et al., 2017; Ke et al., 2020). Briefly, human iPSCs were first digested with accutase and plated on matrigel-coated plates, and were cultured with FP cell induction medium N1 (containing SB431542 (10 μM) and LDN193189 (100 nM), SHH-C24 (100 ng/ml), FGF8 (100 ng/ml), and purmorphamine (2 μM)) from day 0 to day 5. The culture medium was gradually switched to N2 medium from day 5 to day 11 by mixing N1 and N2 in a ratio of 75% (N1): 25% (N2) on days 5 and 6, 50% (N1): 50% (N2) on days 7% and 8%, and 25% (N1): 75% (N2) on days 9 and 10, 100% (N2) on day 11. N1 medium (50 ml) contains 41 ml Knockout DMEM, 7.5 ml Knockout serum replacement, 0.5 ml GlutaMAX, 0.5 ml NEAAs, and 0.5 ml penicillin/streptomycin. N2 medium (50 ml) contained 48.5 ml DMEM/F12 with HEPES buffer/Neural basal, 0.5 ml N2 supplement, 0.5 ml GlutaMAX, and 0.5 ml penicillin/streptomycin. On day 11, FP cells were passaged for expansion and cryopreservation. After expansion of 6 passages, FP cells were disaggregated with accutase and plated to freshly matrigel-coated plates, and the medium was changed to DA induction medium containing NB/B27 supplemented with, GDNF (PeproTech, 20 ng/ml), BDNF (PeproTech, 20 ng/ml), 0.2 mM ascorbic acid (Sigma–Aldrich), DAPT (10 nM; Tocris), cAMP (10 μM, Sigma–Aldrich), and transforming growth factor β3 (1 ng/ml; R&D). And then, cells were dissociated using accutase and diluted to 5 × 105 /ml, and then replated on dishes precoated with poly-D-lysine hydrobromide (PDL) and laminin in DA differentiation medium until the desired maturation stage.

5.16. Drug treatment of iPSC-derived dopamine neurons

All drugs (PJ-34, PDD, ACA, A10 and synthetic polypeptide (PEP, Dentripharm)) were dissolved at 10 mM as stock solutions. The differentiated DA neurons were treated with the drugs at day 15 after the maturation of DA neurons at appropriate concentration and drug-containing culture medium was changed every 4 days.

5.17. Western blotting

Briefly, neurons in culture were collected and lysed with pre-cold 50 μL of RIPA buffer containing 1% PMSF and 1% cocktail (ThermoFisher). Cells were resuspended and ultrasonicated, followed by centrifugation at 12500 g for 20 min at 4 °C. The supernatant was collected and the concentration of each sample was determined using a BCA assay kit (Beyotime Biotechnology) before they were mixed with 5x loading buffer for sample preparation and electrophoresis. The intensity of the bands was analyzed using Image Studio Lite software.

5.18. PLA assay

To detect the direct interaction between Bcl-2 and Mfn2, PLA assay was conducted according to the standard protocol of DuolinkTM in situ Detection Reagents (Sigma Aldrich). Differentiated DA neurons on day 18, SH-SY5Y cells, and mouse brain sections of were fixed with 4% PFA first. Briefly, samples were incubated in a blocking solution for 60 min at 37 °C and washed twice. Anti-Bcl-2 (Santa Cruz, sc-7382) and anti-Mfn2 (Abcam, ab124773) antibodies were diluted with Duolink Antibody Diluent and added to the samples and incubated overnight at 4 °C. Next, samples were washed three times with Wash Buffer A and 1:5 diluted PLUS MINUS PLA probes in antibody diluent were applied and incubated at 37 °C for 1 hr. The probes were washed with Wash Buffer A and the ligation solution was added and incubated at 37 °C for 30 min. After washing, amplification solution was added and incubated at 37 °C for 100 min. The samples were washed with Wash Buffer B, and Duolink InSitu Mounting Medium with DAPI was added to samples. The samples were used for confocal imaging (Zeiss, LSM 880 with Airyscan).

5.19. Ca^{2+} flow cytometry

The Ca^{2+} probe Fluo-4 (Invitrogen, Fluo-4, AM, F14201) was dissolved in extracellular working solution (ECS, containing 130 mM NaCl, 4.6 mM KCl, 2 mM MgCl2, 10 mM HEPES, 5 mM D-Glucose, 100 μM EGTA). The probe solution was pre-heated at 37 °C and added to the wells and incubated for 60 min. The probe solution was discarded and the cells were washed with ECS twice. Another 300 μL-ECS was added to the wells for further incubation for 30 min. ECS was discarded again and cells were digested with pre-heated Accutase for 5 min at 37 °C. The ECS

was discarded and the cells were re-suspended in ECS for flow cytometry experiment (Beckman, DxFLEX). The data were processed with FlowJo 10 software.

5.20. Mitochondria imaging

Mitochondrial morphology was determined upon stained with MitoTracker. Briefly, differentiated DA neurons at day 18 were stained with 500 nM MitoTracker Red (Thermo, M22425) in culture medium for 30 min at 37 °C. Cells were then washed with DPBS. To ensure the desired dopamine neurons were observed, Girk2 antibody (Proteintech, 21647–1–1AP) was used to label vulnerable DA neurons after fixation with PFA were stained with Girk2 antibody for 12 hrs and with second antibody for 12 hrs. The samples were washed three times, and 50% glycerol was added for fluorescent protection. The stained neurons were observed with a confocal microscope (Zeiss, LSM880 with Airy scan, NA 100 nm, 63x oil). The branch length of mitochondria was analyzed with Image J software.

5.21. Immunofluorescence staining

In brief, cells plated on dishes were fixed in 4% paraformaldehyde for 20 min at room temperature , and then cells were blocked in 3% BSA with 0.5% TBST (PBS containing 0.5% Triton X-100) for 1 hr at room temperature after washed with PBS. After the blocking step, cells were incubated overnight with anti-Oct-4 antibody (ab19857, abcam) (1:1000), anti-Tra-1–60 antibody (ab16288, abcam) (1:1000), anti-Nanog antibody (ab109250, abcam)(1:1000), anti-SOX-2 antibody (ab97959, abcam)(1:500) at 4 °C with 1% BSA in 0.1% PBST. On next day, cells were washed in PBS three times, for 5 min each time, and then incubated in secondary antibody (Goat anti-Rabbit IgG (H+L) Highly Cross-Adsorbed Secondary Antibody, Alexa Fluor Plus 488 (A32723, Invitrogen, 1:1000)/Goat anti-Rabbit IgG (H+L) Cross-Adsorbed Secondary Antibody, Alexa Fluor 546 (A11010, Invitrogen, 1:1000). Finally, cells were washed in PBS three times, mounting medium containing DAPI was added for imaging. Fluorescence images were captured using Zeiss LSM 880 with Airyscan with 20X objectives.

5.22. Statistical analysis

Data are processed with GraphPad Prism 8 software and expressed as mean ± s.e.m. Quantitative data distributions were tested for normality using Shapiro–Wilk's test. One-way ANOVA or Two-way ANOVA and appropriate post hoc test were used to compare multiple groups. Two-tail student's t-test was used to reveal a significant individual difference between two groups, and Manny-Whitney test was used instead if the data did not meet the normal distribution. Significance was defined as $P < 0.05$ in all statistical analyses.

CRediT authorship contribution statement

W. Y., L. K. and H. S. designed the study. P. Y. performed the bioinformatic analysis. P. Y., X. H., W. Z. and P. J. carried out the *C. elegans* experiments. P. Y., Q. F., M. H., M. K., Y. L. and X. C. carried out the iPSC-related experiments. Q. F., M. L., X. C. and X. L. carried out mice experiments. C. Z. processed the SEM data. W. Y., P. Y. and Q. F. wrote the manuscript, which was revised by other authors.

Declaration of Competing Interest

The authors declare no competing interests.

Data Availability

Data will be made available on request. The datasets used or analyzed during the current study are available from the corresponding author on reasonable request.

Acknowledgments

We thank Guifeng Xiao, Zhaoxiaonan Lin and Li Liu from the Core Facilities, School of Medicine, Zhejiang University for their technical support. SEM data were collected at Center of Cryo-Electron Microscopy at Zhejiang University. We thank J. Guo for support in facility access and Amira software operation. We thank W. Zou for support and guidance in worm experiments. We thank J. Ji for support in iPSC experiments. We also thank W. Sun and X. Xu for guidance in RNA-seq data analysis. We also thank Y. Tang and L. Lu for helpful discussion and editing of the manuscript. Further support was supported by the following funding: Natural Science Foundation of China 82030108 (WY). National Natural Science Foundation of China 81371302 (WY). Natural Science Foundation of China 31872796 (WY). Natural Science Foundation of China 31471118 (JHL). National Major Special Project on New Drug Innovation of China 2018ZX09711001-004-005 (WY). East-West Cooperation Project 2019BFH02003 (WY). The National Basic Research Program of China 2013CB910204 (WY). The National Basic Research Program of China 2014CB910300 (JHL). Fundamental Research Funds for the Central Universities of China 2016QNA7002 (PY).

Appendix A. Supporting information

Supplementary data associated with this article can be found in the online version at doi:10.1016/j.pneurobio.2023.102530.

References

Anderegg, A., Poulin, J.F., Awatramani, R., 2015. Molecular heterogeneity of midbrain dopaminergic neurons–moving toward single cell resolution. FEBS Lett. 589, 3714–3726.
Berthet, A., Margolis, E.B., Zhang, J., Hsieh, I., Zhang, J., Hnasko, T.S., Ahmad, J., Edwards, R.H., Sesaki, H., Huang, E.J., Nakamura, K., 2014. Loss of mitochondrial fission depletes axonal mitochondria in midbrain dopamine neurons. J. Neurosci. 34, 14304–14317.
Bieri, G., Brahic, M., Bousset, L., Couthouis, J., Kramer, N.J., Ma, R., Nakayama, L., Monbureau, M., Defensor, E., Schule, B., Shamloo, M., Melki, R., Gitler, A.D., 2019. LRRK2 modifies alpha-syn pathology and spread in mouse models and human neurons. Acta Neuropathol. 137, 961–980.
Blesa, J., Trigo-Damas, I., Quiroga-Varela, A., Jackson-Lewis, V.R., 2015. Oxidative stress and Parkinson's disease. Front Neuroanat. 9, 91.
Bloss, T.A., Witze, E.S., Rothman, J.H., 2003. Suppression of CED-3-independent apoptosis by mitochondrial betaNAC in Caenorhabditis elegans. Nature 424, 1066–1071.
Bolam, J.P., Pissadaki, E.K., 2012. Living on the edge with too many mouths to feed: why dopamine neurons die. Mov. Disord. 27, 1478–1483.
Bonora, M., Giorgi, C., Pinton, P., 2022. Molecular mechanisms and consequences of mitochondrial permeability transition. Nat. Rev. Mol. Cell Biol. 23, 266–285.
Breckenridge, D.G., Kang, B.H., Xue, D., 2009. Bcl-2 proteins EGL-1 and CED-9 do not regulate mitochondrial fission or fusion in Caenorhabditis elegans. Curr. Biol. 19, 768–773.
Calixto, A., Chelur, D., Topalidou, I., Chen, X., Chalfie, M., 2010. Enhanced neuronal RNAi in C. elegans using SID-1. Nat. Methods 7, 554–559.
Chikka, M.R., Anbalagan, C., Dvorak, K., Dombeck, K., Prahlad, V., 2016. The mitochondria-regulated immune pathway activated in the c. elegans intestine is neuroprotective. Cell Rep. 16, 2399–2414.
Chipuk, J.E., Moldoveanu, T., Llambi, F., Parsons, M.J., Green, D.R., 2010. The BCL-2 family reunion. Mol. Cell 37, 299–310.
Chung, C.Y., Seo, H., Sonntag, K.C., Brooks, A., Lin, L., Isacson, O., 2005. Cell type-specific gene expression of midbrain dopaminergic neurons reveals molecules involved in their vulnerability and protection. Hum. Mol. Genet 14, 1709–1725.
Chung, S.Y., Kishinevsky, S., Mazzulli, J.R., Graziotto, J., Mrejeru, A., Mosharov, E.V., Puspita, L., Valiulahi, P., Sulzer, D., Milner, T.A., Taldone, T., Krainc, D., Studer, L., Shim, J.W., 2016. Parkin and PINK1 patient iPSC-derived midbrain dopamine neurons exhibit mitochondrial dysfunction and alpha-synuclein accumulation. Stem Cell Rep. 7, 664–677.
Corsi, A.K., Wightman, B., Chalfie, M., 2015. A transparent window into biology: a primer on caenorhabditis elegans. Genetics 200, 387–407.
Damier, P., Hirsch, E.C., Agid, Y., Graybiel, A.M., 1999. The substantia nigra of the human brain. II. Patterns of loss of dopamine-containing neurons in Parkinson's disease. Brain 122 (Pt 8), 1437–1448.
Delivani, P., Adrain, C., Taylor, R.C., Duriez, P.J., Martin, S.J., 2006. Role for CED-9 and Egl-1 as regulators of mitochondrial fission and fusion dynamics. Mol. Cell 21, 761–773.

Di, A., Gao, X.P., Qian, F., Kawamura, T., Han, J., Hecquet, C., Ye, R.D., Vogel, S.M., Malik, A.B., 2011. The redox-sensitive cation channel TRPM2 modulates phagocyte ROS production and inflammation. Nat. Immunol. 13, 29–34.
Di Salvio, M., Di Giovannantonio, L.G., Acampora, D., Prosperi, R., Omodei, D., Prakash, N., Wurst, W., Simeone, A., 2010. Otx2 controls neuron subtype identity in ventral tegmental area and antagonizes vulnerability to MPTP. Nat. Neurosci. 13, 1481–1488.
Eisner, V., Cupo, R.R., Gao, E., Csordas, G., Slovinsky, W.S., Paillard, M., Cheng, L., Ibetti, J., Chen, S.R., Chuprun, J.K., Hoek, J.B., Koch, W.J., Hajnoczky, G., 2017. Mitochondrial fusion dynamics is robust in the heart and depends on calcium oscillations and contractile activity. Proc. Natl. Acad. Sci. USA 114, E859–E868.
Ellis, H.M., Horvitz, H.R., 1986. Genetic control of programmed cell death in the nematode C. elegans. Cell 44, 817–829.
Esposito, G., Di Schiavi, E., Bergamasco, C., Bazzicalupo, P., 2007. Efficient and cell specific knock-down of gene function in targeted C. elegans neurons. Gene 395, 170–176.
Fanczal, J., Pallagi, P., Gorog, M., Diszhazi, G., Almassy, J., Madacsy, T., Varga, A., Csernay-Biro, P., Katona, X., Toth, E., Molnar, R., Rakonczay Jr., Z., Hegyi, P., Maleth, J., 2020. TRPM2-mediated extracellular Ca(2+) entry promotes acinar cell necrosis in biliary acute pancreatitis. J. Physiol. 598, 1253–1270.
Fang, E.F., Hou, Y., Palikaras, K., Adriaanse, B.A., Kerr, J.S., Yang, B., Lautrup, S., Hasan-Olive, M.M., Caponio, D., Dan, X., Rocktaschel, P., Croteau, D.L., Akbari, M., Greig, N.H., Fladby, T., Nilsen, H., Cader, M.Z., Mattson, M.P., Tavernarakis, N., Bohr, V.A., 2019. Mitophagy inhibits amyloid-beta and tau pathology and reverses cognitive deficits in models of Alzheimer's disease. Nat. Neurosci. 22, 401–412.
Fang, Q., Xicoy, H., Shen, J., Luchetti, S., Dai, D., Zhou, P., Qi, X.R., Martens, G.J.M., Huitinga, I., Swaab, D.F., Liu, C., Shan, L., 2021. Histamine-4 receptor antagonist ameliorates Parkinson-like pathology in the striatum. Brain Behav. Immun. 92, 127–138.
Fasano, C.A., Chambers, S.M., Lee, G., Tomishima, M.J., Studer, L., 2010. Efficient derivation of functional floor plate tissue from human embryonic stem cells. Cell Stem Cell 6, 336–347.
Feany, M.B., Bender, W.W., 2000. A Drosophila model of Parkinson's disease. Nature 404, 394–398.
Fedele, S., Collo, G., Behr, K., Bischofberger, J., Muller, S., Kunath, T., Christensen, K., Gundner, A.L., Graf, M., Jagasia, R., Taylor, V., 2017. Expansion of human midbrain floor plate progenitors from induced pluripotent stem cells increases dopaminergic neuron differentiation potential. Sci. Rep. 7, 6036.
Fernandes, H.J.R., Patikas, N., Foskolou, S., Field, S.F., Park, J.E., Byrne, M.L., Bassett, A. R., Metzakopian, E., 2020. Single-Cell Transcriptomics of Parkinson's Disease Human In Vitro Models Reveals Dopamine Neuron-Specific Stress Responses. Cell Rep. 33, 108263.
Ferrer, I., Martinez, A., Blanco, R., Dalfo, E., Carmona, M., 2011. Neuropathology of sporadic Parkinson disease before the appearance of parkinsonism: preclinical Parkinson disease. J. Neural Transm. (Vienna) 118, 821–839.
Firnhaber, C., Hammarlund, M., 2013. Neuron-specific feeding RNAi in C. elegans and its use in a screen for essential genes required for GABA neuron function. PLoS Genet 9 e1003921.
Foehring, R.C., Zhang, X.F., Lee, J.C., Callaway, J.C., 2009. Endogenous calcium buffering capacity of substantia nigral dopamine neurons. J. Neurophysiol. 102, 2326–2333.
Geng, X., Harry, B.L., Zhou, Q., Skeen-Gaar, R.R., Ge, X., Lee, E.S., Mitani, S., Xue, D., 2012. Hepatitis B virus X protein targets the Bcl-2 protein CED-9 to induce intracellular Ca2+ increase and cell death in Caenorhabditis elegans. Proc. Natl. Acad. Sci. USA 109, 18465–18470.
Grimm, J., Mueller, A., Hefti, F., Rosenthal, A., 2004. Molecular basis for catecholaminergic neuron diversity. Proc. Natl. Acad. Sci. USA 101, 13891–13896.
Guzman, J.N., Sanchez-Padilla, J., Wokosin, D., Kondapalli, J., Ilijic, E., Schumacker, P. T., Surmeier, D.J., 2010. Oxidant stress evoked by pacemaking in dopaminergic neurons is attenuated by DJ-1. Nature 468, 696–700.
Hamakawa, M., Hirotsu, T., 2017. Establishment of time- and cell-Specific RNAi in caenorhabditis elegans. Methods Mol. Biol. 1507, 67–79.
Hare, D.J., Double, K.L., 2016. Iron and dopamine: a toxic couple. Brain 139, 1026–1035.
Hengartner, M.O., Horvitz, H.R., 1994. Activation of C. elegans cell death protein CED-9 by an amino-acid substitution in a domain conserved in Bcl-2. Nature 369, 318–320.
Hirsch, E., Graybiel, A.M., Agid, Y.A., 1988. Melanized dopaminergic neurons are differentially susceptible to degeneration in Parkinson's disease. Nature 334, 345–348.
Huang, Y., Winkler, P.A., Sun, W., Lu, W., Du, J., 2018. Architecture of the TRPM2 channel and its activation mechanism by ADP-ribose and calcium. Nature 562, 145–149.
Jackson-Lewis, V., Przedborski, S., 2007. Protocol for the MPTP mouse model of Parkinson's disease. Nat. Protoc. 2, 141–151.
Jiang, L.H., Li, X., Syed Mortadza, S.A., Lovatt, M., Yang, W., 2018. The TRPM2 channel nexus from oxidative damage to Alzheimer's pathologies: an emerging novel intervention target for age-related dementia. Ageing Res Rev. 47, 67–79.
Kam, T.I., Mao, X., Park, H., Chou, S.C., Karuppagounder, S.S., Umanah, G.E., Yun, S.P., Brahmachari, S., Panicker, N., Chen, R., Andrabi, S.A., Qi, C., Poirier, G.G., Pletnikova, O., Troncoso, J.C., Bekris, L.M., Leverenz, J.B., Pantelyat, A., Ko, H.S., Rosenthal, L.S., Dawson, T.M., Dawson, V.L., 2018. Poly(ADP-ribose) drives pathologic alpha-synuclein neurodegeneration in Parkinson's disease. Science 362.
Kamath, T., Abdulraouf, A., Burris, S.J., Langlieb, J., Gazestani, V., Nadaf, N.M., Balderrama, K., Vanderburg, C., Macosko, E.Z., 2022. Single-cell genomic profiling of human dopamine neurons identifies a population that selectively degenerates in Parkinson's disease. Nat. Neurosci. 25, 588–595.
Kamp, F., Exner, N., Lutz, A.K., Wender, N., Hegermann, J., Brunner, B., Nuscher, B., Bartels, T., Giese, A., Beyer, K., Eimer, S., Winklhofer, K.F., Haass, C., 2010. Inhibition of mitochondrial fusion by alpha-synuclein is rescued by PINK1, Parkin and DJ-1. EMBO J. 29, 3571–3589.
Ke, M., Chong, C.M., Zeng, H., Huang, M., Huang, Z., Zhang, K., Cen, X., Lu, J.H., Yao, X., Qin, D., Su, H., 2020. Azoramide protects iPSC-derived dopaminergic neurons with PLA2G6 D331Y mutation through restoring ER function and CREB signaling. Cell Death Dis. 11, 130.
Lakso, M., Vartiainen, S., Moilanen, A.M., Sirvio, J., Thomas, J.H., Nass, R., Blakely, R. D., Wong, G., 2003. Dopaminergic neuronal loss and motor deficits in Caenorhabditis elegans overexpressing human alpha-synuclein. J. Neurochem 86, 165–172.
Liss, B., Striessnig, J., 2019. The potential of L-type calcium channels as a drug target for neuroprotective therapy in Parkinson's disease. Annu Rev. Pharm. Toxicol. 59, 263–289.
Liss, B., Haeckel, O., Wildmann, J., Miki, T., Seino, S., Roeper, J., 2005. K-ATP channels promote the differential degeneration of dopaminergic midbrain neurons. Nat. Neurosci. 8, 1742–1751.
Lu, Y., Rolland, S.G., Conradt, B., 2011. A molecular switch that governs mitochondrial fusion and fission mediated by the BCL2-like protein CED-9 of Caenorhabditis elegans. Proc. Natl. Acad. Sci. USA 108. E813-822.
Maddox, J.W., Khorsandi, N., Gleason, E., 2018. TRPC5 is required for the NO-dependent increase in dendritic Ca(2+) and GABA release from chick retinal amacrine cells. J. Neurophysiol. 119, 262–273.
Malko, P., Jiang, L.H., 2020. TRPM2 channel-mediated cell death: An important mechanism linking oxidative stress-inducing pathological factors to associated pathological conditions. Redox Biol. 37, 101755.
Malpartida, A.B., Williamson, M., Narendra, D.P., Wade-Martins, R., Ryan, B.J., 2021. Mitochondrial dysfunction and mitophagy in Parkinson's disease: from mechanism to therapy. Trends Biochem Sci. 46, 329–343.
Markvicheva, K.N., Bilan, D.S., Mishina, N.M., Gorokhovatsky, A.Y., Vinokurov, L.M., Lukyanov, S., Belousov, V.V., 2011. A genetically encoded sensor for H2O2 with expanded dynamic range. Bioorg. Med Chem. 19, 1079–1084.
Matsuda, W., Furuta, T., Nakamura, K.C., Hioki, H., Fujiyama, F., Arai, R., Kaneko, T., 2009. Single nigrostriatal dopaminergic neurons form widely spread and highly dense axonal arborizations in the neostriatum. J. Neurosci. 29, 444–453.
Metzstein, M.M., Stanfield, G.M., Horvitz, H.R., 1998. Genetics of programmed cell death in C. elegans: past, present and future. Trends Genet 14, 410–416.
Mor, D.E., Sohrabi, S., Kaletsky, R., Keyes, W., Tartici, A., Kalia, V., Miller, G.W., Murphy, C.T., 2020. Metformin rescues Parkinson's disease phenotypes caused by hyperactive mitochondria. Proc. Natl. Acad. Sci. USA 117, 26438–26447.
Mouatt-Prigent, A., Agid, Y., Hirsch, E.C., 1994. Does the calcium binding protein calretinin protect dopaminergic neurons against degeneration in Parkinson's disease? Brain Res 668, 62–70.
Nagarajan, A., Ning, Y., Reisner, K., Buraei, Z., Larsen, J.P., Hobert, O., Doitsidou, M., 2014. Progressive degeneration of dopaminergic neurons through TRP channel-induced cell death. J. Neurosci. 34, 5738–5746.
Nicklas, W.J., Youngster, S.K., Kindt, M.V., Heikkila, R.E., 1987. MPTP, MPP+ and mitochondrial function. Life Sci. 40, 721–729.
Pacelli, C., Giguere, N., Bourque, M.J., Levesque, M., Slack, R.S., Trudeau, L.E., 2015. Elevated mitochondrial bioenergetics and axonal arborization size are key contributors to the vulnerability of dopamine neurons. Curr. Biol. 25, 2349–2360.
Papanicolaou, K.N., Khairallah, R.J., Ngoh, G.A., Chikando, A., Luptak, I., O'Shea, K.M., Riley, D.D., Lugus, J.J., Colucci, W.S., Lederer, W.J., Stanley, W.C., Walsh, K., 2011. Mitofusin-2 maintains mitochondrial structure and contributes to stress-induced permeability transition in cardiac myocytes. Mol. Cell Biol. 31, 1309–1328.
Parent, M., Parent, A., 2006. Relationship between axonal collateralization and neuronal degeneration in basal ganglia. J. Neural Transm. Suppl. 85–88.
Perez-Pinzon, M.A., Stetler, R.A., Fiskum, G., 2012. Novel mitochondrial targets for neuroprotection. J. Cereb. Blood Flow. Metab. 32, 1362–1376.
Pham, A.H., Meng, S., Chu, Q.N., Chan, D.C., 2012. Loss of Mfn2 results in progressive, retrograde degeneration of dopaminergic neurons in the nigrostriatal circuit. Hum. Mol. Genet 21, 4817–4826.
Qi, H., Price, B.D., Day, T.A., 2019. Multiple roles for mono- and poly(ADP-Ribose) in regulating stress responses. Trends Genet 35, 159–172.
Raghunatha, P., Vosoughi, A., Kauppinen, T.M., Jackson, M.F., 2020. Microglial NMDA receptors drive pro-inflammatory responses via PARP-1/TRMP2 signaling. Glia 68, 1421–1434.
Rolland, S.G., Lu, Y., David, C.N., Conradt, B., 2009. The BCL-2-like protein CED-9 of C. elegans promotes FZO-1/Mfn1,2- and EAT-3/Opa1-dependent mitochondrial fusion. J. Cell Biol. 186, 525–540.
Sawin, E.R., Ranganathan, R., Horvitz, H.R., 2000. C. elegans locomotory rate is modulated by the environment through a dopaminergic pathway and by experience through a serotonergic pathway. Neuron 26, 619–631.
Schultz, W., 2007. Behavioral dopamine signals. Trends Neurosci. 30, 203–210.
Segura-Aguilar, J., Paris, I., Munoz, P., Ferrari, E., Zecca, L., Zucca, F.A., 2014. Protective and toxic roles of dopamine in Parkinson's disease. J. Neurochem 129, 898–915.
Shu, X., Lev-Ram, V., Deerinck, T.J., Qi, Y., Ramko, E.B., Davidson, M.W., Jin, Y., Ellisman, M.H., Tsien, R.Y., 2011. A genetically encoded tag for correlated light and electron microscopy of intact cells, tissues, and organisms. PLoS Biol. 9 e1001041.
Singatulina, A.S., Hamon, L., Sukhanova, M.V., Desforges, B., Joshi, V., Bouhss, A., Lavrik, O.I., Pastre, D., 2019. PARP-1 Activation Directs FUS to DNA Damage Sites to Form PARG-Reversible Compartments Enriched in Damaged DNA. Cell Rep. 27, 1809–1821 e1805.
Sorrentino, V., Romani, M., Mouchiroud, L., Beck, J.S., Zhang, H., D'Amico, D., Moullan, N., Potenza, F., Schmid, A.W., Rietsch, S., Counts, S.E., Auwerx, J., 2017.

Enhancing mitochondrial proteostasis reduces amyloid-beta proteotoxicity. Nature 552, 187–193.
Surmeier, D.J., 2007. Calcium, ageing, and neuronal vulnerability in Parkinson's disease. Lancet Neurol. 6, 933–938.
Szabo, G., Bahrle, S., Stumpf, N., Sonnenberg, K., Szabo, E.E., Pacher, P., Csont, T., Schulz, R., Dengler, T.J., Liaudet, L., Jagtap, P.G., Southan, G.J., Vahl, C.F., Hagl, S., Szabo, C., 2002. Poly(ADP-Ribose) polymerase inhibition reduces reperfusion injury after heart transplantation. Circ. Res 90, 100–106.
Takahashi, N., Kuwaki, T., Kiyonaka, S., Numata, T., Kozai, D., Mizuno, Y., Yamamoto, S., Naito, S., Knevels, E., Carmeliet, P., Oga, T., Kaneko, S., Suga, S., Nokami, T., Yoshida, J., Mori, Y., 2011. TRPA1 underlies a sensing mechanism for O2. Nat. Chem. Biol. 7, 701–711.
Tatton, N.A., Kish, S.J., 1997. In situ detection of apoptotic nuclei in the substantia nigra compacta of 1-methyl-4-phenyl-1,2,3,6-tetrahydropyridine-treated mice using terminal deoxynucleotidyl transferase labelling and acridine orange staining. Neuroscience 77, 1037–1048.
Tavernarakis, N., Wang, S.L., Dorovkov, M., Ryazanov, A., Driscoll, M., 2000. Heritable and inducible genetic interference by double-stranded RNA encoded by transgenes. Nat. Genet 24, 180–183.
Thomas, B., Banerjee, R., Starkova, N.N., Zhang, S.F., Calingasan, N.Y., Yang, L., Wille, E., Lorenzo, B.J., Ho, D.J., Beal, M.F., Starkov, A., 2012. Mitochondrial permeability transition pore component cyclophilin D distinguishes nigrostriatal dopaminergic death paradigms in the MPTP mouse model of Parkinson's disease. Antioxid. Redox Signal 16, 855–868.
Thompson, L., Barraud, P., Andersson, E., Kirik, D., Bjorklund, A., 2005. Identification of dopaminergic neurons of nigral and ventral tegmental area subtypes in grafts of fetal ventral mesencephalon based on cell morphology, protein expression, and efferent projections. J. Neurosci. 25, 6467–6477.
Tiklova, K., Bjorklund, A.K., Lahti, L., Fiorenzano, A., Nolbrant, S., Gillberg, L., Volakakis, N., Yokota, C., Hilscher, M.M., Hauling, T., Holmstrom, F., Joodmardi, E., Nilsson, M., Parmar, M., Perlmann, T., 2019. Single-cell RNA sequencing reveals midbrain dopamine neuron diversity emerging during mouse brain development. Nat. Commun. 10, 581.
Trimmer, P.A., Swerdlow, R.H., Parks, J.K., Keeney, P., Bennett Jr., J.P., Miller, S.W., Davis, R.E., Parker Jr., W.D., 2000. Abnormal mitochondrial morphology in sporadic Parkinson's and Alzheimer's disease cybrid cell lines. Exp. Neurol. 162, 37–50.
Ungless, M.A., Grace, A.A., 2012. Are you or aren't you? Challenges associated with physiologically identifying dopamine neurons. Trends Neurosci. 35, 422–430.
Vyas, S., Matic, I., Uchima, L., Rood, J., Zaja, R., Hay, R.T., Ahel, I., Chang, P., 2014. Family-wide analysis of poly(ADP-ribose) polymerase activity. Nat. Commun. 5, 4426.
Wang, L., Fu, T.M., Zhou, Y., Xia, S., Greka, A., Wu, H., 2018. Structures and gating mechanism of human TRPM2. Science 362.
Wang, Q., Wang, M., Choi, I., Ho, L., Farrell, K., Beaumont, K.G., Sebra, R., Crary, J.F., Davis, D.A., Sun, X., Zhang, B., Yue, Z., 2022. Single-cell Transcriptomic Atlas of the Human Substantia Nigra in Parkinson's Disease. bioRxiv, 2022.2003.2025.485846.
Wang, Y., Kim, N.S., Haince, J.F., Kang, H.C., David, K.K., Andrabi, S.A., Poirier, G.G., Dawson, V.L., Dawson, T.M., 2011. Poly(ADP-ribose) (PAR) binding to apoptosis-inducing factor is critical for PAR polymerase-1-dependent cell death (parthanatos). Sci. Signal 4 ra20.
Wang, Y., An, R., Umanah, G.K., Park, H., Nambiar, K., Eacker, S.M., Kim, B., Bao, L., Harraz, M.M., Chang, C., Chen, R., Wang, J.E., Kam, T.I., Jeong, J.S., Xie, Z., Neifert, S., Qian, J., Andrabi, S.A., Blackshaw, S., Zhu, H., Song, H., Ming, G.L., Dawson, V.L., Dawson, T.M., 2016. A nuclease that mediates cell death induced by DNA damage and poly(ADP-ribose) polymerase-1. Science 354.
Wei, Y., Lu, M., Mei, M., Wang, H., Han, Z., Chen, M., Yao, H., Song, N., Ding, X., Ding, J., Xiao, M., Hu, G., 2020. Pyridoxine induces glutathione synthesis via PKM2-mediated Nrf2 transactivation and confers neuroprotection. Nat. Commun. 11, 941.
Xia, R., Mei, Z.Z., Mao, H.J., Yang, W., Dong, L., Bradley, H., Beech, D.J., Jiang, L.H., 2008. Identification of pore residues engaged in determining divalent cationic permeation in transient receptor potential melastatin subtype channel 2. J. Biol. Chem. 283, 27426–27432.
Xu, S., Chisholm, A.D., 2014. C. elegans epidermal wounding induces a mitochondrial ROS burst that promotes wound repair. Dev. Cell 31, 48–60.
Yu, P., Xue, X., Zhang, J., Hu, X., Wu, Y., Jiang, L.H., Jin, H., Luo, J., Zhang, L., Liu, Z., Yang, W., 2017. Identification of the ADPR binding pocket in the NUDT9 homology domain of TRPM2. J. Gen. Physiol. 149, 219–235.
Yu, P., Liu, Z., Yu, X., Ye, P., Liu, H., Xue, X., Yang, L., Li, Z., Wu, Y., Fang, C., Zhao, Y.J., Yang, F., Luo, J.H., Jiang, L.H., Zhang, L., Zhang, L., Yang, W., 2019. Direct Gating of the TRPM2 Channel by cADPR via Specific Interactions with the ADPR Binding Pocket. Cell Rep. 27, 3684–3695 e3684.
Yu, X., Xie, Y., Zhang, X., Ma, C., Liu, L., Zhen, W., Xu, L., Zhang, J., Liang, Y., Zhao, L., Gao, X., Yu, P., Luo, J., Jiang, L.H., Nie, Y., Yang, F., Guo, J., Yang, W., 2021. Structural and functional basis of the selectivity filter as a gate in human TRPM2 channel. Cell Rep. 37, 110025.
Zhou, P., Homberg, J.R., Fang, Q., Wang, J., Li, W., Meng, X., Shen, J., Luan, Y., Liao, P., Swaab, D.F., Shan, L., Liu, C., 2019. Histamine-4 receptor antagonist JNJ7777120 inhibits pro-inflammatory microglia and prevents the progression of Parkinson-like pathology and behaviour in a rat model. Brain Behav. Immun. 76, 61–73.
Zou, J., Ainscough, J.F., Yang, W., Sedo, A., Yu, S.P., Mei, Z.Z., Sivaprasadarao, A., Beech, D.J., Jiang, L.H., 2013. A differential role of macrophage TRPM2 channels in Ca(2)(+) signaling and cell death in early responses to H(2)O(2). Am. J. Physiol. Cell Physiol. 305, C61–C69.